UNIVERSIDAD NACIONAL AUTÓNOMA DE MÉXICO

PROGRAMA DE MAESTRÍA Y DOCTORADO EN INGENIERÍA

FACULTAD DE INGENIERÍA

FLOW THROUGH AXI-SYMMETRIC CONTRACTIONS

T E S I S

QUE PARA OPTAR POR EL GRADO DE:

MAESTRO EN INGENIERÍA

MECÁNICA –TERMOFLUIDOS

P R E S E N T A:

SERVANDO RUIZ RODRÍGUEZ

DIRECTOR:

DR. GABRIEL ASCANIO GASCA

2011

JURADO ASIGNADO:

Presidente:	DR. JAIME CERVANTES DE GORTARI
Secretario:	DR. FRANCISCO JAVIER SOLORIO ORDAZ
Vocal:	DR. GABRIEL ASCANIO GASCA
1er. Suplente:	DR. JOSÉ ROBERTO ZENIT CAMACHO
2do. Suplente:	DR. LUIS MEDINA TORRES

Lugar donde se realizó la tesis:

CENTRO DE CIENCIAS APLICADAS Y DESARROLLO TECNOLÓGICO, UNIVERSIDAD NACIONAL AUTÓNOMA DE MÉXICO, CIUDAD UNIVERSITARIA, MEXICO D. F., MEXICO.

TUTOR DE TESIS:
DR. GABRIEL ASCANIO GASCA

FIRMA

DEDICATORIA

En primer lugar y principalmente quiero dedicar este trabajo a la persona gracias a la que he recibido educación, principios y valores: MI MADRE, ELVIRA RODRÍGUEZ RAMOS, no sólo por ser mi madre, pero por habernos sacado adelante a mí y a mis hermanos y ser la persona más importante para mí. Gracias por todo el apoyo y cariño pero sobre todo por haberme soportado tanto tiempo. En segundo lugar quiero dedicar el mi trabajo a mis hermanos Sergio y Joel porque sé que siempre podremos confiar entre nosotros y ayudarnos sin importar cómo sea nuestra relación. También quisiera dedicar este trabajo a la memoria de mis familiares que ya no están conmigo en este mundo.

Dedico además a mis amigos Alberto, Gabriela, Juan Carlos, Karla, Martín, Mauricio, Octavio, Ramsés pues son las personas con las que más he convivido es durante esta etapa de mi vida y que sé seguiremos echando relajo mucho tiempo. Dedico además a mis demás amigos y amigas a los que se les aprecia a pesar de que no figuren en esta lista.

AGRADECIMIENTOS

Nuevamente quiero agradecer a mi madre por todo lo que me ha dado en la vida ya que sin ella yo no hubiera logrado lo que he logrado. Quiero agradecer en segundo lugar a mi tutor, el Dr. Gabriel Ascanio, por toda la confianza que me tuvo y el apoyo que me dio durante mi estancia en el CCADET, siempre con amabilidad, gracias a lo cual me fue posible realizar este trabajo. Gracias al CCADET por su estancia y a los técnicos y trabajadores de dicho centro que me ayudaron así como a mis maestros durante el posgrado por todo lo que me enseñaron. Gracias al Dr. Solorio Ordaz y al Dr. Zenit Camacho por permitirme utilizar los Laboratorios de Termofluidos de la Facultad de Ingeniería y de Reología del Instituto de Investigaciones en Materiales respectivamente. Del primer me gustaría agradecer a Rafa y del segundo a Ernesto por la ayuda y amistad que me brindaron mientras estuve dando lata. Al Dr. Luis Medina Torres del laboratorio de Reometría de la Facultad de Química por su ayuda en la caracterización de las sustancias. Al Dr. Enrique Soto por toda la ayuda que me brindó en la parte final del trabajo, enseñarme a utilizar el reómetro y corregirme los últimos aspectos de mi escrito. A CONACYT por haberme apoyado económicamente mientras duraron mis estudios. Gracias finalmente a mis compañeros del CCADET que me ayudaron en algún momento de mi estancia. Nuevamente gracias a mis amigos por su apoyo, pero sobre todo por los momentos y horas y días y días de relajo. No los menciono para evitar olvidos pues como cualquiera que me haya conocido sabrá, siempre hay algo que se me olvida.

¡GRACIAS EN GENERAL A TODOS LOS QUE ME RODEAN!

INDEX

List of figures

ABSTRACT

In this work, the flow behaviour of Newtonian and non-Newtonian fluids through two axi-symmetric contractions (an abrupt contraction and a parabolic one) has been analysed for diverse volumetric flows rates. The parabolic profile was developed in previous works with the aim of reducing, even fully eliminating, secondary flows (recirculation and stagnation zones) near the contraction.

PIV (particle image velocimetry) technique was used to obtain the flow fields with a Nd:Yag laser plane as illumination source having an energy of 120 mJ and 532 nm wavelength and hollow glass particles of 10 μm of diameter as tracers. The volumetric flow rates were measured with a test tube and a chronometer. Flow Manager Software from Dantec Dynamics Co. was used to acquire images and process them to obtain numerical data of flow maps. Numerical data was then processed with MATLAB software.

For the parabolic contraction, good agreement with the literature and the theory was found, having large vortices for the elastic fluids. For the parabolic contraction, no secondary flow was observed in any experiment even with relatively high elastic fluids. In spite of that, separation of the streamlines from the wall was noticed for the elastic fluid which could bring inaccuracies in the measurement of the extensional viscosity when using the Binding's Analysis (Binding, 1987). On the other hand, the parabolic contraction was found to be appropriate to measure the extensional viscosity of inelastic fluids.

1. Introduction

1.1. Literature survey

Flow through contractions, like any other geometry change in pipes, is important to fluid mechanics due to the large number of applications involving these types of geometries in both industrial and research. Flow fields and pressure drop in contractions strongly depend on the geometry, flow parameters and fluid rheology. Contractions can be classified in three types: axi-symmetric, planar and square (Figure 1.1.).

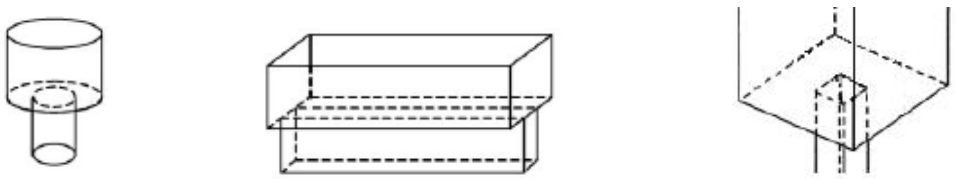

Figure 1.1. Axi-symmetric (left), planar (middle) and square (right) contraction.

One application of the flow through contraction is the volumetric flow measurement in pipes. For that purpose, there are three basic forms with international standards for the Bernoulli's obstructions (axi-symmetric); the nozzle (long-radius or short-radius), the thin-plate orifice and the Venturi tube. As the fluid flows through a contraction, it is accelerated to satisfy the continuity equation or mass conservation by keeping constant the volumetric flow. When applying continuity and Bernoulli equations for incompressible steady frictionless flow, the pressure drop and mean velocity (or the volumetric flow) can be estimated as a function of the pressure gradient:

$$p_0 = p_{\mathrm{u}} + \frac{1}{2}\rho \cdot V_{\mathrm{u}}^2 = p_{\mathrm{c}} + \frac{1}{2}\rho \cdot V_{\mathrm{c}}^2 \tag{1}$$

$$Q = \frac{\pi}{4} D_u^2 V_{\mathrm{u}} = \frac{\pi}{4} D_c^2 V_{\mathrm{c}} = A_c V_c \tag{2}$$

Eliminating V_u and from (1) and (2), we obtain

$$\frac{Q}{A_c} = V_c \approx \left[\frac{2 \cdot (p_u - p_c)}{\rho \cdot (1 - d_c^4 d_u^4)} \right]^{1/2} \tag{3}$$

where: $p_u - p_c = \Delta p$, is the pressure drop; d_u and V_u are the upstream pipe diameter and the mean velocity; d_c, A_c and V_c are the diameter, the transversal area and the mean velocity in the contraction, respectively; ρ is the fluid density; and Q is the volumetric flow.

Nevertheless, the fluid can be contracted to a diameter d_c' (*vena contracta*) lower than d_c but in practice they are considered to be equal, thus, some errors can be expected. A dimensionless correction factor, C_d, is added to compensate them and to account the friction; this correction factor is specific for each type of contraction and is a function of the Reynolds number, Re_d (d_u as the characteristic length), and the contraction ratio, RC. Considering $RC = R_u / R_c = d_u / d_c$:

$$Q = A_c \cdot V_c = C_d \cdot A_c \cdot \left[\frac{2 \cdot (P_u - P_c)\rho}{1 - RC^4} \right]^{1/2} \tag{4}$$

The different values for the discharge coefficients can be found in most of fluids engineering text books the three geometries.

Another quite important application is observed in the design of rheometers to measure the extensional viscosity. This material property is very important for many industrial applications and processing operations like fibber spinning, thermoforming, blow molding, foam production, injection, inkjet printing, fertiliser spraying and others. In addition, this kind of flow is able to orient polymer molecules and asymmetric particles which have a strong effect on the final product properties. Besides, it is the most used

technique to measure the elongational viscosity because it is the easiest manner to create extensional flow mostly with low-viscosity fluids with all the three geometry contractions (Mitsoulis et al, 2003; Rothstein and McKinley,1999; James and Chandler, 1991; De la Valle et al, 2002; Ascanio et al, 2002, Alves et al,2005; Mongruel and Cloitre, 2003; Kahn et al, 2007; Schuberth and Münstedt, 2008; Olson and Fuller, 2000; Sato, 1995; Baris, 2001 and others).

The method is often called Entrance Flow (Macosko, 1994). As the fluid experiences the area reduction, the streamlines converge and the flow dissipates certain quantity of extra energy through the walls because of the viscous effects that is expressed as an entrance excess pressure drop, Δp_{en}. There is large shear deformation near the walls and large extensional deformation near the centre, being the former the responsible for the excess of pressure drop, which can be used, together with the flow, rate to estimate the extensional viscosity by using one of the previously established relationships (Sink flow, Metzner and Metzner; Cogswell, 1972; Binding, 1987 and others). Tremblay (1989) combined the methods developed by Binding and Cogswell to determine the extensional viscosity of polymers. Other works reporting the through sudden and profiled contractions were reported by James and Chandler (1990), Feigl *et al* (2003) and Zatloukal et al (2002). James and Chandler (1990) made a mathematical analysis to obtain a geometry in which they could have constant elongational rate and it was achieved experimentally for Newtonian fluids. Feigl et al (2003) and Zatloukal et al (2002) proposed a new material parameter (entrance viscosity) and an ”effective entry length correction” for the Cogswell and Binding’s models. Another important recent analytical study is the one of Lubansky *et*

al. (2007), who gave a solution when high Trouton ratios are used and found that the vortex behaviour strongly depends on the fluid's characteristic relaxation time.

Astarita y Greco (1968) and Astarita *et al.* (1968) performed an experimental and numerical analysis to measure the pressure drop in both Newtonian and non-Newtonian fluids flowing through contractions with both fluids. They found that for Newtonian fluids, the dimensionless pressure drop depends only on the Reynolds number for values lower than 146, being independent at higher values. They found also that for fluids with elasticity, the pressure drop goes down when the Reynolds increases and that it is proportional to the concentration of the fluid. More recently, Mitsoulis y Hatzikiriakos (2003) made an experimental and numerical research to measure the pressure drop in conical contractions by varying the entrance from 10° to 150° using fused polypropylene. They found that the pressure drop depends more on the shear strain for small angles and that elongational strain domains the pressure drops for angle higher than 45°. Besides, they found that in abrupt contractions (180°) the elongational viscosity has the highest influence in the pressure drops and the vortices length.

One drawback of this kind of geometry is the appearance of secondary flows especially for low volumetric flows. Vortices can be found in a contraction as corner vortex and lip vortex (figure 1.2.). One of the first studies to visualise vortices was made by Nguyen and Boger (1979) with streak photography. After that, vortices have been observed with several techniques, like PIV (Rothstein and McKinley, 2001; Oliveira et al, 20057), LDV (Mitsoulis et al, 2003; Hertel et al, 2008; Schubert and Münstedt, 2008), streakline photography (Zitloukal et al, 2002; Alves et al, 2005), birrefrigerance (Schubert and

Münstedt, 2008). Also, since the last decade when Computational Fluid Dynamics (CFD) became a powerful tool, a lot of researchs have been made (Baloch et al 1996; Zirnsak and Boger, 1998; Rothstein and McKinley, 2001; Zatloukal et al, 2002; Alves et al,2003; Dorpinghaus and Baird, 2003; Feigl et al, 2003; Clemeur et al, 2004; Alves et al, 2005; Afonso and Pinho, 2006; Alves and Pool, 2007; Belblidia et al, 2007; Oliveira et al, 2007; Oliveira et al, 2008; etc.).

Figure 1.2. Vortices in a contraction.

It has been seen in all these papers that length of vortices depends on the contraction ratio (RC), the volumetric flow and the fluid rheology. When using an inelastic fluid, little corner vortices are observed in the corner of the contraction and its length decreases as the inertial effect increases (Reynolds number). Quite different behaviour for elastic fluids occur: vortices length increases when increasing the volumetric flow if the elasticity becomes significant as pointed out by Binding (1987). It has been found than there is an asymptotic behaviour of the inelastic Newtonian vortices length when decreasing the Reynolds number and that only corner vortices appear, besides, there is no change in the dimensionless size with RC in a wide range (Nguyen and Boger, 1979) and they present no instabilities. For a time, researches about contractions were focused on 4:1 contractions which are very limitating with the practical applications that can be found as it was pointed out by Nigen and Walters (2002) and by Alves et al (2004).

Also, vortex generation is different in each one of the three geometries (planar, axi-symmetric and squared). Nigen and Walters (2002) made a study to investigate the differences between the planar and the axi-symmetric contractions and the influence of the contraction ratio, CR. They found that for CR between 2 and 40, elasticity has a lower influence on the flow than in the axi-symmetric case, being difficult distinguish between Newtonian and Boger fluids of the same shear viscosity in planar configurations. In both cases, vortices length increase when increasing CR. Alves *et al* (2004) found that for CR > 4 on planar contractions, vortex enhancement follows a lip-vortex mechanism and found that corner vortex characteristics scale with the upstream length scale and with the Deborah number ($DE = \lambda \cdot U_u/H_u$, where λ is the characteristic relaxation time of the fluid, U_u and H_u the average velocity and the half-height of the channel upstream, respectively) divided by CR and that lip vortex scales with the downstream length scale and De when using CR higher than 10. Rothstein and McKinley (2001) found that for large CR (4:1, 8:1) instabilities at high Deborah numbers appear and for lower CR (2:1) the flow was stable even at very high Deborah numbers. Also, for CR = 2, an elastic lip vortex was found and for 4 < CR a vortex corner appeared. Alves et al (2005) found that in the case of square contractions, the flow is highly three-dimensional showing vortices with Newtonian and viscoelastic fluids which tend to be pushed to the corner when the inertia is increased for the first ones and increase for the viscoelastic fluids. Instabilities in the flow at high volumetric flows were found also.

Others numerical and experimental investigations have been made to estimate the flow field, the pressure drop and the vortices generation with both fluids, Newtonian and non-Newtonian, for abrupt contractions in the three types geometries where it has been seen

that the behaviour can be highly different between them when using similar fluids and volumetric flows. Alves *et al.* (2005) and in Rood et al (2007) summarised the results obtained with the three geometries with Newtonian and non-Newtonian fluids. However, little information has been found with smooth contractions to vortex genesis with another type of geometry like rounded and chamfer contractions.

Papathanasiou y Kamal (1990) made numerical simulations on contractions-expansions with rounded and chamfer corners and with a parabolic profile. They found that the vortices disappeared at small Reynolds numbers and that they were visible only at higher ones. Also they showed that the higher the diameter the higher the Reynolds number to start seeing the vortices and that in the parabolic profiles there were large vortices at the exit of the contraction and that the length of these zones depended on the fluid rheology. Baloch *et al.* (1994) investigated the extensional effects with both contractions, abrupt and rounded. They proposed a model that ignores the shear dependence and the memory effects and made numerical simulations with the model and using two fluids with different rheology and compared them with experimental results. They found that the recirculation zones disappear with the rounded corners at low Reynolds and that when the flow rate is increased, the vortices appear.

In the 70s a converging channel was first proposed; Cogswell (1978) proposed a converging geometry to measure the extensional viscosity. However, several years passed until work made with converging channel were made. One of the first works to create pure extensional flow in a smooth contraction was made on earliest 90´s by James (1991). He found an analytical solution for flow in a converging channel for Reynolds numbers in the

range of 10^2 to 10^3 for an axisymmetric channel and obtain that the shape given by R^2z = constant, where R is the channel radius at the axial distance z. It is a pseudosimilarity solution of the axial momentum equation, and its accuracy was gauged by comparison to other results obtaining an accuracy of about 5% in comparisons with experimental results. James and Chandler (A-1990) used the method of James (1991) to develop an extensional rheometer for copolymer solutions of PMMA in an organic solvent (Polymethylmethacrylate in Dowanol DPM). They achieved a purely extensional core flow with constant rate of extension by using high Reynolds obtaining no secondary motion (vortices) and made an analysis to show that the pressure drop is equal to sum of the normal stress difference in the core and a term involving N_2. They made the study first obtaining the flow for an inelastic power-law fluid to obtain the pressure drop, to obtain after the corresponding shear-thinning fluid profile and pressure drop and with them the C_p as a function of RE_n, necessary to obtain the extensional viscosity. Their principal inaccuracy was the term involving N_2 but they were able to measure the extensional viscosity as a function of the deformation. Then, James and Chandler (B-1990) used it to measure the extensional viscosity of the international test fluid M1. They obtained an error of ±25%. After, Shirakashi *et al.* (1997) measured the velocity profiles using laser Doppler Velocimetry (LDV) for water and Polyacrilamide solutions in the converging channel of James (1991). They found that this geometry generated a constant extensional rates (shear-free cores in velocity profiles for Reynolds between 100 and 150 and centreline velocity at each flow rate increases linearly along the axis) for both fluids ad that velocity profiles predicted by James (1991) quasi-similarity solution agreed with the water ones but not with a elastic fluid like the PAA.

Collier (1994) made a work similar to the previous one with a converging smooth contraction but also with lubricated walls. Feigl et al (2003) generalized a technique to measure extensional viscosity (James et al, 1990; Collier, 1994). In that technique, extruding a material through a cylindrical, semi-hyperbolic converging die with polymer melts and solutions is involved with finite element technique. That shape produced a shear-free, or nearly shear-free, flow and found that the viscosity is a sum of an effective elongational viscosity $\eta_{ef} = -\Delta P/(\varepsilon\ \varepsilon)_h$, that involved the change in pressure over the die, the volumetric flow and the Hencky strain determined by the geometry and a term involving a change in enthalpy that can be neglected. They said also that the shape of the die produces elongational flow only when the fluid fully slips along the wall, eliminating shear effects, or if the shear effects are restricted to a thin layer along the wall, achieved only with the use of lubricants, and in its absence, a nearly shear-free flow occurs only when there is slip along the wall. They concluded there were advantages when using semi-hyperbolic dies because they are "relatively easy and inexpensive to perform" and that "taking the pressure at the outlet to be atmospheric provides the pressure difference, while the volumetric flow rate and the geometry of the die provide the elongation rate $\dot{\varepsilon}$ and the Hencky strain $\varepsilon_h = 2\ \ln(Ro/Re)$, $\eta_{ef} = -\Delta P/(\varepsilon\ \varepsilon)_h$ is immediately computed". Additionally, higher elongation rates can be reached with these types of geometry.

Poole *et al.* (2005) performed a numerical and experimental research of flow of viscoelastic fluid through and abrupt planar expansion preceded by a gradual contraction (RC = 8), which consisted of a circumference arc concave followed by an convex one (the concave arc radius were double than the convex) by using laser anemometry (LDA) with shear-thinning liquids (aqueous solution of PAA, 0.05% weight). First, they found the

expected parabolic profile, but later in the contraction they found “unexpected velocity overshoot” near the wall that grows as it goes downstream. They called those high velocity zones founded near the wall, higher than the velocity in the centreline, “cat’s ears” and attributed them to “the first and second normal-stress differences produced which increase with increasing shear rate”. On the expansion, they found a three-dimensional flow.

The first attempt to obtain, predict and explain the cat’s ears was made by Afonso and Pinho (2006). They identified the conditions necessary to observe the overshoots and found a good “qualitative” agreement. Poole et al (2007) made and experimental and numerical investigation on the same geometry as Poole *et al.* (2005) but varying the concentration of the aqueous solutions of PAA. On the expansion they found that when the concentration is increased, the length of the recirculation zones decreases “dramatically”. They showed that “the exact shape and magnitude of the cat’s ears are found to be Reynolds number and Deborah number dependent” and, by using the PTT model (Phan-Thien and Tanner), they could obtain numerically the cat’s ears but they were not identical in magnitude that the experimental, founding instabilities when increasing N_2 on the model, something necessary to obtain the overshoots.

Alves y Poole (20007) made a numerical research on divergent flow in smooth contractions with a geometry based on that of Poole *et al.* (2005) (in this case with the same radius, equal to the difference between the contractions ratio, r_A R – r) for creeping, isothermal and incompressible viscoelastic flow. They used the upper-convected Maxwell (UCM) model and finite-volume numerical method with the QUICK scheme (Leonard, 1979) whereas there are no singularities because it is not an abrupt contraction; CR varied

(16, 4 and 2). They observed that at higher contraction ratio, the effect of elasticity on the flow was small and divergent flow was not observed, so they demonstrated that divergent flow is more likely to be observed in small CR and that there is a Deborah number (that linearly varies with the CR) in which, above it, a purely elastic instability sets in. According to them, divergent flow occurs when the Trouton ratio goes to its maximum value. They could obtain in a more accurate way than Poole et al (2007) the cat's ears. They concluded also that 'the use of smooth contractions offer many advantages over the typical abrupt ones, aside from the absence of vortex enhancement'.

Oliveira *et al.* (2007) studied numerical and experimentally the Newtonian flow through a microfabricated hyperbolic planar contraction with μPIV and they obtained good agreement between numerical and experimental results. They found that on that scale, the flow has important 3D effects (so, the 2D approximation is not enough), for geometries with very low-aspect ratio, Hele-Shaw approximation is good and 2-D viscous flow did not appear; pressure drop across the contraction varied approximately linearly with Re. However, there was no constant deformation along the centreline of the geometry and the wall effects were not negligible, but with higher strains these effects decrease but viscous shearing contribution makes difficult to obtain purely extensional flows. They concluded that the use of viscoelastic fluid should reduce this problem because of the development of additional elastic stress resulting from the elongational flow. They obtained quite similar behaviour between the experiment and the macroescale ones with the maximum velocity at the centreline and fully developed flow far upstream entering in a region where it accelerates as the contraction plane is reached.

In this work, flow through a parabolic axi-symmetric contraction is going to be study to analyse its usefulness in a new orifice rheometer to measure the elongational viscosity. Flow pattern will be compared with an abrupt contraction. The abrupt geometry is the same as reported by Ascanio et al (2002), who characterised coating fluids (see Figure 1.3), while the parabolic contraction is the same as the one reported by Naranjo (2010) and it was designed primarily to eliminate the recirculation zones and obtain a wide range of deformation rates and shear viscosities for the design of a rheometer for measuring extensional viscosity by using the Binding's analysis. It is used to validate experimentally the elimination of the recirculation zones and obtain the flow fields and how the rheology influences the experimental results.

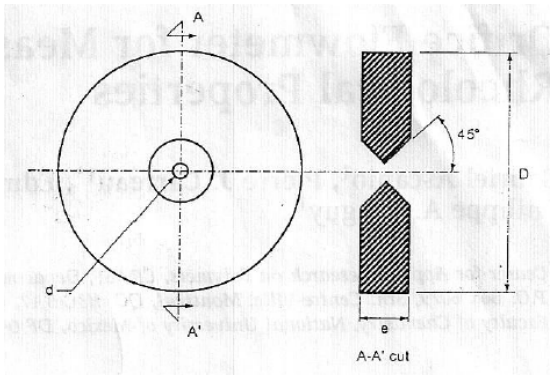

Figure 1.3. Contraction profile used by Ascanio *et al* (2002).

Hence, this work is structured in the following way: Chapter 2 describes the theoretical background; Chapter 3 deals with the experimental setup describing the visualisation technique and the fluids investigated; Chapter 4 shows and discusses the results and finally the conclusions and work proposed for the new future.

1.2. Objectives

1.2.1. General Objective

- *Analyse the behaviour of laminar steady flow with Newtonian and non-Newtonian fluids through abrupt and parabolic contractions.*

1.2.2. Specific Objectives

- *To obtain the flow fields near the contraction by using the particle image velocimetry technique (PIV)*

- *To analyse the influence of fluid rheology on the hydrodynamics of fluids flowing through parabolic contractions.*

2. Theoretical background

Figure 2.1 shows the streamlines and velocity profile for uniaxial extension and shear flow (Macosko, 1994).

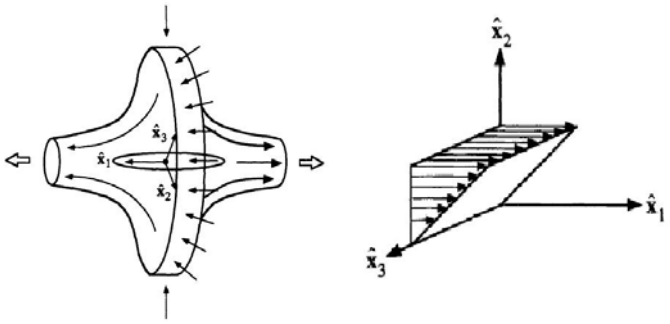

Figure 2.1Extensional and shear flow.

The velocity gradient tensor and the deformation rate tensors are given, respectively, by

$$L_{ij} = (\nabla v)^T = \begin{bmatrix} \dot{\varepsilon} & 0 & 0 \\ 0 & -\dot{\varepsilon}/2 & 0 \\ 0 & 0 & -\dot{\varepsilon}/2 \end{bmatrix}, \; 2D_{ij} = \nabla v + (\nabla v)^T = \begin{bmatrix} 2\dot{\varepsilon} & 0 & 0 \\ 0 & -\dot{\varepsilon} & 0 \\ 0 & 0 & -\dot{\varepsilon} \end{bmatrix} \tag{5}$$

$$\text{and } L_{ij} = (\nabla v)^T = \begin{bmatrix} 0 & \dot{\gamma} & 0 \\ 0 & 0 & 0 \\ 0 & 0 & 0 \end{bmatrix}, \; 2D_{ij} = \nabla v + (\nabla v)^T = \begin{bmatrix} 0 & \dot{\gamma} & 0 \\ \dot{\gamma} & 0 & 0 \\ 0 & 0 & 0 \end{bmatrix}. \tag{6}$$

In uniaxial extension, $\dot{\varepsilon}$ corresponds to the direction where extensional deformation occurs, $\hat{x}_1$. When calculating the vorticity tensor, **W,** it can be seen that there is no vorticity in uniaxial extensional flow, $W_{ij} = L_{ij} + L_{ji} = 0$.The stress tensor, **T**, is:

$$T = \begin{bmatrix} T_{11} & T_{12} & T_{13} \\ T_{21} & T_{22} & T_{23} \\ T_{31} & T_{32} & T_{33} \end{bmatrix}, \tag{7}$$

and it is related to the strain tensor. The stress tensor is symmetrical and can be written as the sum of two parts, one corresponding to the hydrostatic pressure and one called as to the viscous stress tensor, $\mathbf{T} = -p\mathbf{I} + \boldsymbol{\tau}$. All the deformation effects are found on the last term, $\boldsymbol{\tau}$, but it cannot be directly measured. So, to eliminate *p,* normal stress differences are used:

$$N_1 = T_{11} - T_{22} = \tau_{11} - \tau_{22} \tag{8}$$

$$N_2 = T_{22} - T_{33} = \tau_{22} - \tau_{33} \tag{9}$$

In general terms, the shear viscosity is defined as

$$\eta(\dot{\gamma}) = \frac{\tau_{12}(\dot{\gamma})}{\dot{\gamma}}, \tag{10}$$

and the extensional viscosity as

$$\begin{aligned} \mu_1^+(\dot{\varepsilon}, t) &= \frac{T_{11} - T_{22}}{2(2+m)\dot{\varepsilon}} \\ \mu_2^+(\dot{\varepsilon}, t) &= \frac{T_{22} - T_{33}}{2(1+2m)\dot{\varepsilon}} \end{aligned} \tag{11}$$

and the rate tensor for a general extensional deformation is:

$$\mathbf{D} = \dot{\varepsilon}\begin{bmatrix} 1 & 0 & 0 \\ 0 & m & 0 \\ 0 & 0 & -(1+m) \end{bmatrix} \tag{12}$$

Where, *m* is equal to -0.5, 1 or 0 for uniaxial, equibiaxial and planar extension, respectively. It can be seen that μ_2^+ is defined only in equibiaxial and planar extension, however, measurements in this type of extensional flows are not very common. Then, the extensional viscosity is usually defined as

$$\eta_e = \frac{T_{11} - T_{22}}{\dot{\varepsilon}} \tag{13}$$

In our case, the flow is a combination of both types of flows, so that vorticity should be considered. The velocity gradient tensor in cylindrical coordinates is given by

$$L_{ij} = (\nabla v)^T = \begin{bmatrix} \frac{\partial v_r}{\partial r} & \frac{1}{r}\frac{\partial v_r}{\partial \theta} - \frac{v_\theta}{r} & \frac{\partial v_r}{\partial z} \\ \frac{\partial v_\theta}{\partial r} & \frac{1}{r}\frac{\partial v_\theta}{\partial \theta} + \frac{v_r}{r} & \frac{\partial v_\theta}{\partial z} \\ \frac{\partial v_z}{\partial r} & \frac{1}{r}\frac{\partial v_r}{\partial r} & \frac{\partial v_z}{\partial z} \end{bmatrix} \tag{14}$$

Assuming laminar flow, symmetry on ϑ, null angular velocity and symmetry on z,

$$\frac{\partial}{\partial \theta} = 0 \;\&\; v_\theta = 0\,, \tag{15}$$

and substituting (15)into (14), the strain tensor ***D*** becomes

$$2\mathbf{D} = (\mathbf{L} + \mathbf{L}^{\mathbf{T}}) = \begin{bmatrix} 2\frac{\partial v_r}{\partial r} & 0 & \frac{\partial v_z}{\partial r} + \frac{\partial v_r}{\partial z} \\ 0 & 2\frac{v_r}{r} & 0 \\ \frac{\partial v_z}{\partial r} + \frac{\partial v_r}{\partial z} & 0 & 2\frac{\partial v_z}{\partial z} \end{bmatrix} \tag{16}$$

with, $D_{zz} = \frac{\partial v_z}{\partial z} = \varepsilon$ and $2D_{rz} = \left(\frac{\partial v_z}{\partial r} + \frac{\partial v_r}{\partial z}\right) = \dot{\gamma}$,being $W_{rz} = -W_{zr} = \frac{\partial v_r}{\partial z} - \frac{\partial v_z}{\partial r}$, the only component of vorticity.

The stress tensor is related with the deformation tensor and it depends on the type of fluid. The simplest one is the Newtonian fluid:

$$\boldsymbol{\tau} = \eta \cdot 2 \cdot \mathbf{D}, \text{ or } \mathbf{T} = -p\mathbf{I} + \eta 2\mathbf{D} \tag{17}$$

This expression is the Newton's law in three dimensions. Substituting 2**D** from pure shear flow, Eq. (6), gives

$$\mathbf{T}_{12} = \boldsymbol{\tau}_{12} = \eta\dot{\gamma} \text{ (Newton's law of viscosity)} \tag{18}$$

Substituting 2**D** for uniaxial extension, eq. (5), into the stress tensor, it gives

$$T_{11} = -p + 2\eta\dot{\varepsilon} \tag{19}$$

$$T_{22} = T_{33} = -p - \eta\dot{\varepsilon} \ , \tag{20}$$

neglecting surface tension effects we obtain that $T_{22} = T_{33} = 0$, so

$$-p = \eta\dot{\varepsilon} \Rightarrow T_{11} = 3\eta\dot{\varepsilon} \tag{21}$$

Recalling the definition of extensional viscosity, eq. (13), we obtain

$$\eta_u = 3\eta \ , \tag{22}$$

that is often called the Trouton ratio and it holds for Newtonian fluids and for some non-Newtonian fluids, like polymer melts, at very low shear rates.

Another widely used relation is the power law model,

$$\tau_{ij} = k\left|II_{2D}\right|^{(n-1)/2}(2D_{ij}) \ , \tag{23}$$

where $\left|II_{2D}\right|$, is the second invariant of the rate tensor, **D**, and in simple shear it gives

$$\tau_{12} = \tau_{21} = k\dot{\gamma}^n \quad \text{or} \quad \eta = k\dot{\gamma}^{n-1} \tag{24}$$

When $n = 1$, then $k = \eta$ and we have the Newtonian case.

Another very used non-Newtonian model is the Cross Model, a four constant model with a Newtonian part at low and high shear rates and a power law region in the middle; that is:

$$\frac{\eta - \eta_\infty}{\eta_0 - \eta_\infty} = \frac{1}{1 - (C \cdot \dot{\gamma})^m}$$

There are some other models that relate the stress tensor, **T**, with the rate tensor, **D**, that can also describe the viscoelastic effects (Maxwell, Second-Order Fluid,Upper-Convected Maxwell, PTT model, etc.) which also can be pretty much elaborated. However, they will not be showed here.

Several analyses have been made to calculate the extensional viscosity with an orifice rheometer. Metzner and Metzner (1970) and Cogswell (1972) made two important analyses, later extended by Cogswell (1978). Metzner and Metzner (the sink flow analysis, analogy with a point sink) assumed a purely extensional flow. For the axisymmetric case, using spherical coordinates and continuity equation and considering Figure 2.2, it gives

$$v_r = \frac{Q}{A}; \quad \mathrm{v}_\theta = v_\phi$$

Considering now the isosceles triangle made with the angle ϕ (half-angle of convergence) and using cosines' law, the area is

$$A = \pi 2r^2(1-\cos\phi)$$

giving the radial velocity and extension rate at the orifice

$$v_r = \frac{Q}{2\pi r^2(1-\cos\phi)}$$

$$\dot{\varepsilon} = \frac{dv_r}{dr} = \frac{Q\sin^3\phi}{\pi R_c^3(1-\cos\phi)}$$

Pressure drop is assumed to be equal to the normal stress difference, $\tau_{11}-\tau_{22} \approx \Delta p$ and so, the apparent extensional viscosity, eq. (13), is given by

$$\eta_{u,a} = \frac{\Delta p}{\dot{\varepsilon}}$$

However, ϕ varies highly with flow rate, especially with high elastic fluids, and it predicts a maximum at $\phi = 60°$ that does not have a physical meaning. Tremblay (1989) proposed another sink flow analysis for large convergence angles having

$$\dot{\varepsilon} = \frac{Q}{\pi R_c^3 (2 - \cos\theta)}; \quad \dot{\gamma} = \frac{FQ}{2\pi R_c^3 \cos\theta (1 + \cos\theta)}$$

$$\Delta p = \frac{\pi R_c^3 (\eta \dot{\gamma}^2 + \eta_u \dot{\varepsilon}^2)}{Q}$$

with $F = R_c/\Delta$ to be determined experimentally, Δ is a characteristic length upstream where it can be considered sink flow.

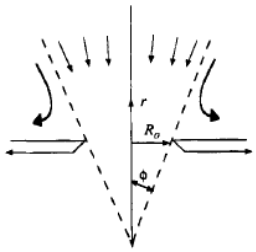

Figure 2.2. Streamlines for sink flow analysis.

Cogswell (1972) made a force balances for shear and normal stresses on a conical section of length, δl, (Figure 2.3) and substituted the stresses by viscosities and integrated them in the whole section. He considered the pressure drop as the sum of both, shear, Δp_s, and extensional, Δp_e, contributions and then minimised the infinite sum of pressure drops along the converging region to obtain p_0, having

$$\Delta p_s = \frac{2k}{3n \tan\theta} \left(\frac{4Q}{\pi R_c^3} \right)^n \left[1 - \left(\frac{R_c}{R_u} \right)^{3n} \right] \quad \text{and} \quad \Delta p_s = \frac{\eta_e \tan\theta}{3} \left(\frac{4Q}{\pi R_c^3} \right) \left[1 - \left(\frac{R_c}{R_u} \right)^3 \right]$$

for constant η_e. The extension rate is

$$\mathcal{E} = \frac{\tau_{11} - \tau_{22}}{\lambda}, \tag{25}$$

$$\tau_{11} - \tau_{22} = \frac{3}{8}(n+1)p_0, \tag{26}$$

$$\lambda = \frac{9(n+1)^2}{32\eta}\left(\frac{P_0}{\dot{\gamma}_a}\right)^2 \tag{27}$$

where $\dot{\gamma}_a = 4Q/\pi R_c^3$ is the apparent shear rate. Or, substituting (26) and (27) into (25)

$$\mathcal{E} = \frac{\eta\dot{\gamma}_a^2}{2(\tau_{11} - \tau_{22})} = \frac{\tau_w\dot{\gamma}_a}{2(\tau_{11} - \tau_{22})}$$

where τ_w is the wall shear stress.

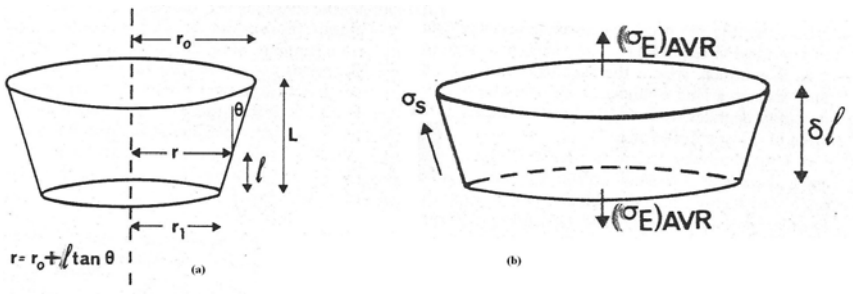

Figure 2.3. Cogswell analysis considerations: (a) Geometrical characteristics; (b) Stresses.

Another important analysis, and the one in which the rheometer with the parabolic profile studied here is based, is the one made by Binding and co-workers (Binding, 1987; Binding and Walters, 1988; Figure 2.4). They made an energy balance assuming three contributions (shear-viscous dissipation, extensional-viscous dissipation and inertial effects) and obtained the profile that minimised the power consumption by using variational principles assuming that elastic effects were not as important as the viscous effects.

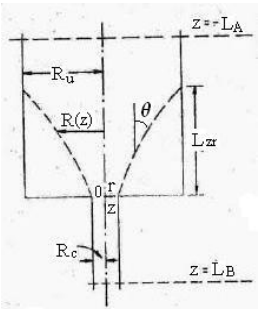

Figure 2.4. Flow idealization for Binding's Analysis.

It was considered that the fluid flows through the surface defined by *r=R(z)* with the angle θ small and slowly varying. It was assumed also that, because axial velocity in *r=R(z)* is very much lower than the velocity on the axis (*r*=0), the axial velocity in a given plane is determined as if there were fully developed flow in a pipe of width *R(z)*, so, considering it and using mass conservation equation:

$$v_z = \frac{(3n+1)Q}{(n+1)\pi R^2}\left\{1-\left(\frac{r}{R}\right)^{1+1/n}\right\},$$

$$v_r = \frac{(3n+1)Qr}{(n+1)\pi R^3}\left\{1-\left(\frac{r}{R}\right)^{1+1/n}\right\}\frac{dR}{dz}$$

Meanwhile, the stress fields are written in terms of the shear and extensional viscosity, both having power-law behaviour, Eq. (23) and $\eta_e = l\dot{\varepsilon}^{t-1}$. Evaluating Eq. (16), neglecting terms $(dR/dz)^2$ and $d^2R/dz^2$and with

$$T = \begin{bmatrix} -p+\tau_{rr} & 0 & \tau_{rz} \\ 0 & \tau_{\theta\theta} & 0 \\ \tau_{rz} & 0 & \tau_{zz} \end{bmatrix}$$

it is possible to measure the rate of work, $\dot{w} = \mathbf{T}:\mathbf{D} = (\tau_{zz}-\tau_{rr})\dot{\varepsilon} + \tau_{rz}\dot{\gamma} + (\tau_{\theta\theta}-\tau_{rr})D_{\theta\theta}$, where the last term is neglected of the quasi-unidirectional nature of the flow. The energy supplied in an infinitesimal element

$$\delta\dot{E} = 2\pi\left\{\int_0^R \left(\dot{w}_s + \dot{w}_e\right) r dr\right\}\delta z + \delta k = f\left(R, \frac{dR}{dz}\right)\delta z \tag{28}$$

where, δk, is the increasing net rate of kinetic energy in the element (inertial component), $w_s = \eta\dot{\gamma}^2$, is the shear viscous dissipation and $w_e = \eta_e \varepsilon^2$, is the extensional viscous dissipation(extensional viscosity defined by Eq. (13)) and where it can be seen that the energy is a function of the profile R. Then, the total power consumption in the converging section is $\dot{E} = \int_{-lv}^{0} f\left(R, \frac{dR}{dz}\right) dz$. Then, variational principles are used to chose the profile $H(z)$ that requires the lower power consumption satisfying $\frac{\partial}{\partial H'}\left(\frac{f}{H'}\right) = 0,$ with $H'=dH/dz$, and it is obtained

$$\left(\frac{dR}{dz}\right)^{t+1} = \frac{k(n+1)^{t+1}}{lt(3n+1)n^n I_{nt}}\left[\frac{(3n+1)Q}{\pi R^3}\right]^{n-t}, \tag{29}$$

with $I_{nt} = \int_0^1 \left\{ abs\left[2 - \left(\frac{3n+1}{n}\right)\phi^{1+1/n}\right]^{t+1} \phi d\phi \right\}$ giving for the power consumption.

$$\dot{E} = \frac{2kQ(t+1)^2}{3t^2(1+n)^2}\left[\frac{lj(3n+1)n^t I_{nt}}{k}\right]^{1/1+t} \dot{\gamma}_{R_0}^{t(n+1)/1+t}\left(1 - \alpha^{3t(n+1)/1+t}\right) + \frac{3\rho Q^3(3n+1)^2(1-\alpha)^4}{2(2n+1)(5n+3)\pi^2 R_u^4},$$

with $\dot{\gamma}_{R_0} = (3n+1)Q/n\pi R_u^3$.

Then a energy balance is written as

$$(p_A - p_B)Q = p'_{(-L_A,-L_v)}Q + \dot{E} + p'_{(0,-L_B)}Q \tag{30}$$

where $p_A - p_B$ is the pressure difference upstream and downstream the contraction where the flow is fully developed and $p'_{(z_1,z_2)}$ is the pressure that would be between two planes if

the flow were fully developed. If we define the entry pressure, $p_e = p_A - p_B - p'_{(-L_A,0)} - p'_{(0,-L_B)}$, as the actual pressure drop less the fully-developed pressure, then, substituting in (30)

$$p_e = \dot{E}/Q - p'_{(-L_v,0)}$$

which, for this axi-symmetric case, integrating(28) and neglecting inertia leads to

$$p_e = \frac{2k(1+t)^2}{3t^2(1+n)^2}\left\{\frac{lt(3n+1)n^t I_{nt}}{k}\right\}^{1/(1+t)} \dot{\gamma}_{Rc}^{t(n+1)/(1+t)}\left\{1-\alpha^{3t(n+1)/(1+t)}\right\}. \qquad (31)$$

Then, to calculate the extensional viscosity, a plot of log(p_e) against log(Q) with an expected slope of $t(n+1)/(1+t)$ to obtain t and then l is obtained directly with Eq. (30). The analysis then can be extended to profile nozzles considering the natural convergence angle with the one of the nozzle at each section of the converging nozzle, Figure 2.5. If the natural angle of convergence, ϑ_n, is smaller than the natural angle of convergence, θ, then the minimisation procedure must be done and if $\theta_n > \theta$ then the energy power consumption must use the equation of the nozzle to be solved.

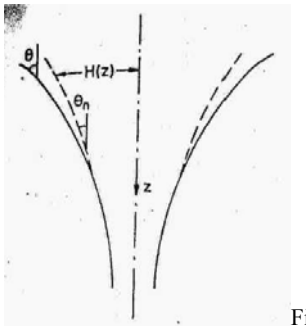

Figure 2.5. Converging flow in a profiled nozzle.

3. Methodology

3.1. Flow geometry

Figures 3.1 shows the geometric profiles of the different contractions considered in this work, the abrupt contractions and the parabolic one, respectively, showing the most important measures of each one.

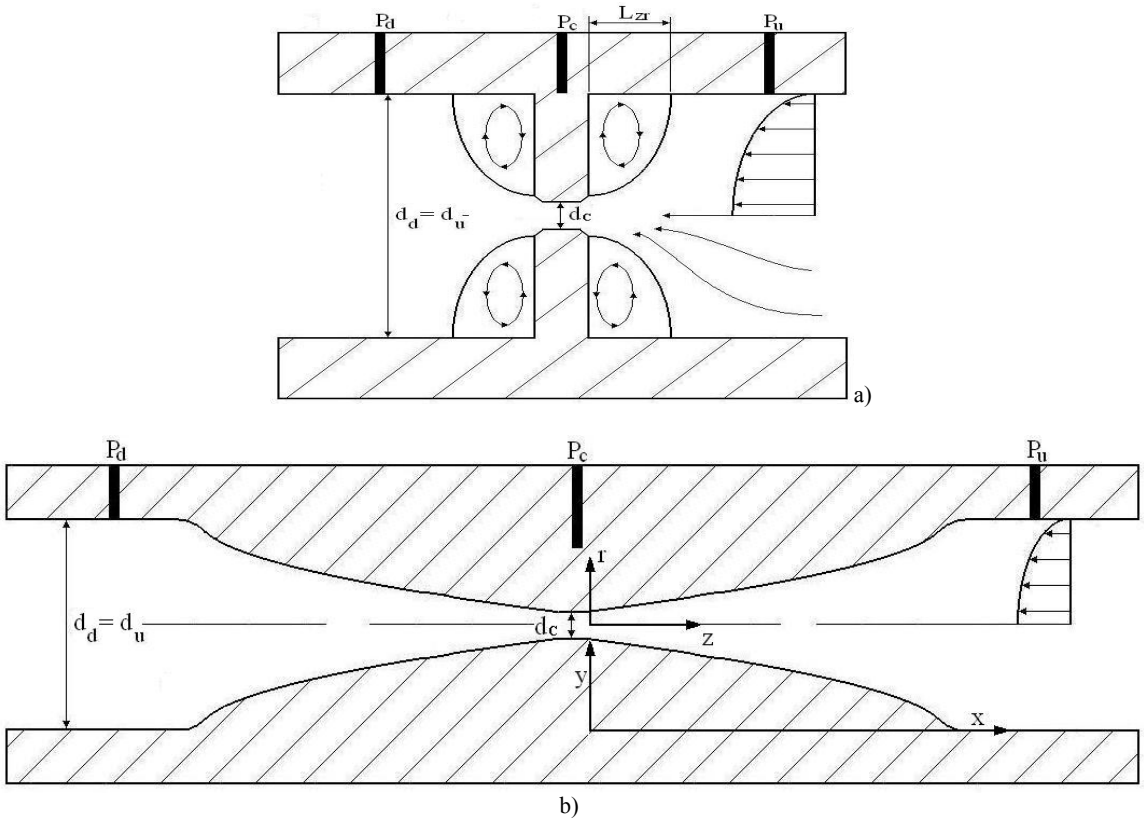

Figure 3.1. Contraction profile: a) abrupt; b) parabolic.

Both contractions have the same contraction ratio, RC = 8; this is done to obtain a better comparison between them. d_U = 38 mm, is the diameter upstream and downstream the contraction and d_u = 4.75 mm, is the contraction diameter in both cases. p_u, p_c and p_d, are the pressures upstream, in the contraction and downstream, respectively. p_u and p_d are

measured one diameter upstream and downstream, respectively. L_{ZR} is the length of the recirculation zones that goes from the wall of the contraction to the point where the flow separate from the pipe's wall. In the case of the parabolic contraction, only the upstream part of the contraction is going to be studied. The dimensionless vortex length with the major diameter, d_u, is

$$x_{ZR} = \frac{L_{ZR}}{d_u}$$

The parabola of the contraction has its focus on the wall of the pipe and opens toward the wall of the contraction. It joins to the pipe with a 7.5 cm radius and his equation on the coordinate system *x*-*y* (Fig. 3.1 b) is:

$$x = -0.23332 \cdot y^2 + 64.48784$$

So, the radius decreases in z with the relation:

$$R = \begin{cases} 19 - \sqrt{\dfrac{64.48784 - z}{0.23332}}, \cdots 0 \le z \le 63.3921 \\ 11.5 + \sqrt{7.5^2 - (z - 68.6656)^2}, \cdots 63.3921 < z \le 68.6656 \end{cases} \tag{32}$$

$$\text{with} \left(\frac{dR}{dz} \right)_{contraction} = \begin{cases} \dfrac{1}{0.46664(19 - R)}, \cdots 0 \le z \le 63.3921 \\ \dfrac{68.6656 - z}{R - 11.5}, \cdots 63.3921 < z \le 68.6656 \end{cases} \tag{33}$$

It is seen that the strain rate along the geometry is not constant, but due to the absence of vortices, an approximate estimation of the strain rate along the centreline is possible like in Alves and Pool (2007). It has to be to pointed out that according to the Binding's analysis, the angle of the profile and the natural angle of convergence has to be compared, so, to avoid the separation of the streamlines from the wall, the next inequality must be satisfied

$$\left(-\frac{dR}{dz}\right) \geq \left(-\frac{dR}{dz}\right)_{contraction} \tag{34}$$

3.2. Visualization technique. Particle Image Velocimetry (PIV).

PIV is a non-intrusive method which allows obtaining quantitatively and qualitatively the velocity vector field of a flow. PIV allows also obtain the instantaneous turbulent flow field with the aim of investigate the fundamental mechanisms of the turbulence end extract its special structure, and with that, obtain the vorticity and deformation fields (Lai, 1996). It is based on the particles tracing and has a very simple operation principle; it consists of taking two consecutive images of the flow where the displacements ΔX and ΔY are taken in a known time period Δt (Figure 3.2). Knowing the position in an interrogation or study area on each exposure and the time between them, a statistical method based on auto-correlation or cross-correlation is used to calculate a vector for each zone by dividing the displacements between the interval Δt. To get sure that it is a good approximation, the displacements have to be small and by choosing a small Δt compared with the Taylor microscale of the Lagrangian velocity field.PIV equipment consists basically of a pulsed or continuous high power laser used as an illumination source, an optical arrangement used for creating a light sheet, the region of study, which contains the working fluid and the particle tracers that are seeded to the study region and a camera to obtain the images that is placed perpendicularly with respect to the laser sheet (Figure 3.2).

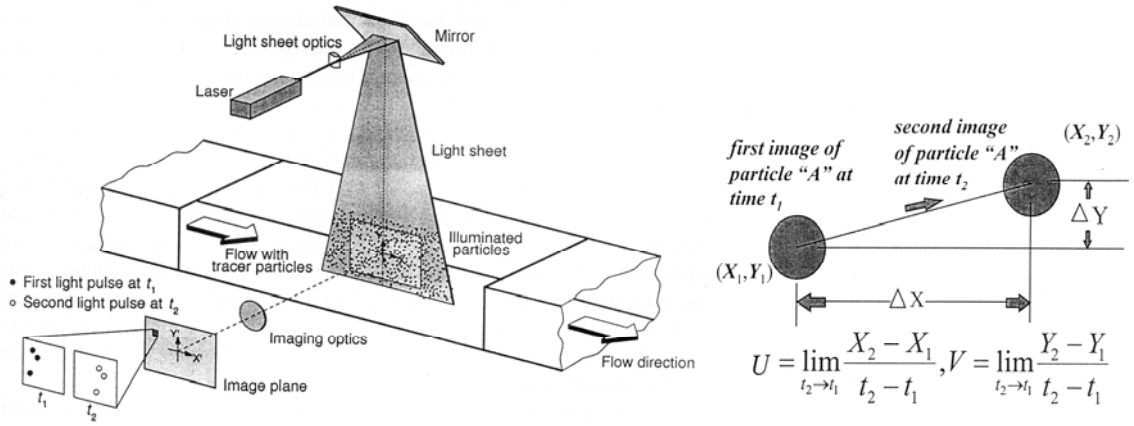

Figure 3.2. PIV operating principle.

Tracers seeded in the flow (in this case, 0.5 μm hollow particles of glass covered with silver) are small enough and with such a density that they follow the flow dynamics. The illumination source acts as a photographic flash by providing light pulses and the tracers scatter the light. The digital camera, which usually is synchronized with the laser, catches at least two exposures, which are then used for the measurement of velocity. A video camera can be used also to obtain the images. A computer system is used for recording such exposures on several frames, which are split in the interrogation areas necessaries.

3.3. Experimental Setup

Figure 3.3 shows the experimental setup. First, we have a twenty-litre container tank were the fluid to be tested is stored and is connected to the entrance pipe made of brass by using flanges. The entrance pipe (30-cm length and with diameter D_1) is long enough to make sure that the flow is fully developed and is made of brass. The different contractions are connected to the end of the entrance pipe set by using flanges too. After that, the exit pipe, made of brass too, is located. Next, a plastic hose is connected to the exit pipe and there is a

gate valve in it that is used to regulate the flow. The hose leads the flow to a centrifugal pump (Finish Thompson, model AC4) driven by a 1/3 HP DC motor (Baldor CDP3420-V12) which is managed with a DC SCR Control (Baldor BC141) to regulate the motor's velocity and with it, the volumetric flow. At the exit, the fluid is led again with a plastic hose to the container tank to close the circuit. To measure the volumetric flow, a test tube and a chronometer are used by taking the time necessary to have 0.5 litres of the fluid. Volumetric flow was measured before, during and after each recording to ensure there was no change. Neoprene seals in all the flanges are used to avoid fugues. Laminar, steady, uncompressible and isothermic flow was considered in this work.

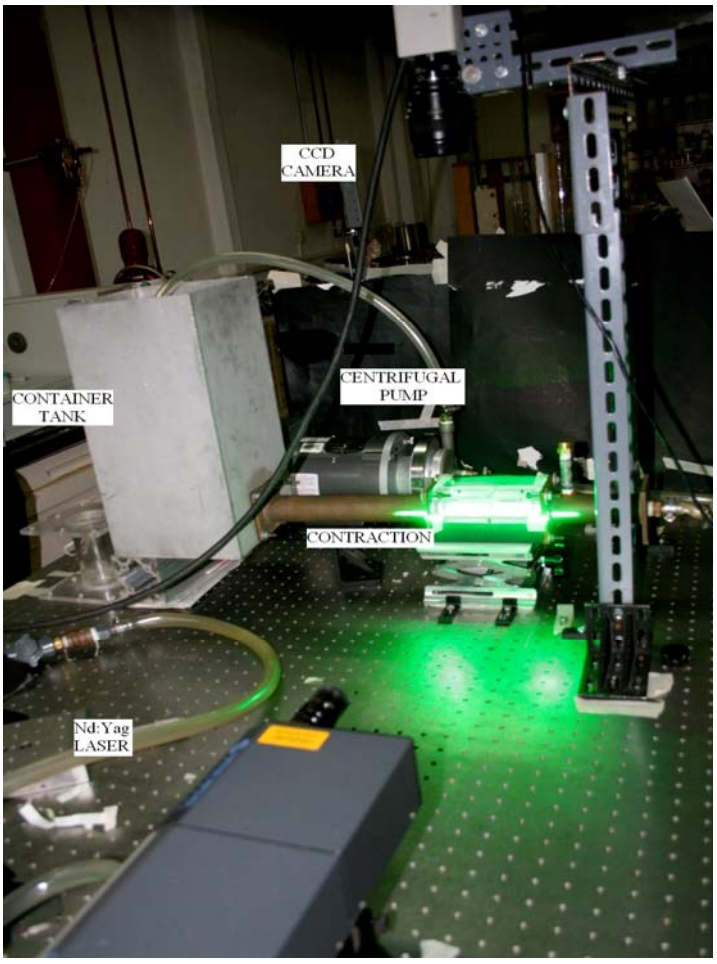

Figure 3.3. Experimental set-up.

Figure 3.4 shows the contractions used in this work, they are made in acrylic to allow PIV visualizations. A square jacket surrounds the contraction, so that the laser light sheet is projected on a planar surface to avoid optical distortion due to the curvature. The abrupt contraction was made in one piece while the parabolic contraction was made in four parts, due to manufacturing complications, with CNC using MASTERCAM software.

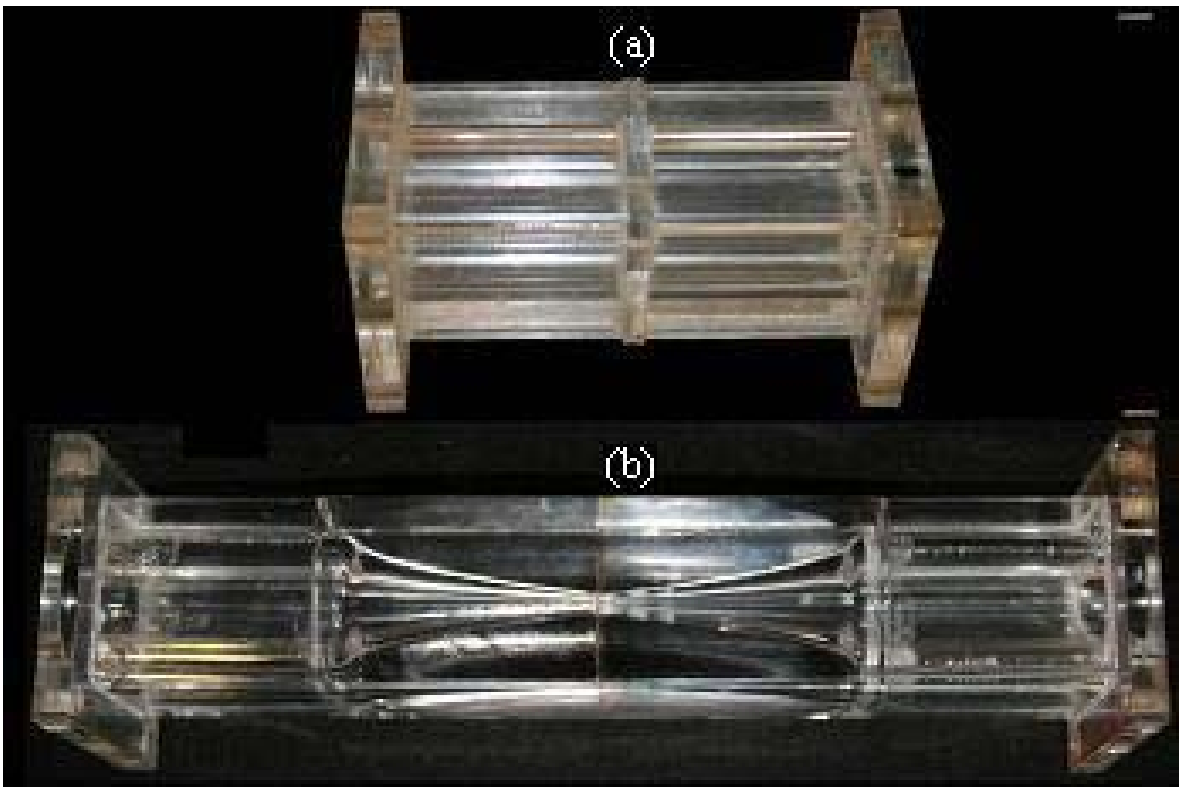

Figure 3.4. Contraction: (a) Abrupt; (b) Parabolic.

3.4. Fluids

Four different fluids were used in the experiment. Aqueous solution of Polyethylene Glycol (PG) at 25% wt (CL 20000 S from Clariant Co.) having a dynamic viscosity of 0.24

[Pa·s] was used as Newtonian fluid. On the other hand, the following non-Newtonian fluids were used:

- PA: Aqueous solution of polyacrilamide at 1% wt
- CMC: Aqueous solution of carboxymehtyl cellulose (Mw = 2000 g/mol) at 2 % wt
- CMC-PG: Aqueous solution of polyethylene glycol at 25% wt plus carboxymethyl cellulose (Mw= 50,000 g/mol) at 0.5% wt

Substances were characterised with an Aanton Paar Physica Rheometer MC 301 with a 50mm-diameter cone-and-plate geometry with an angle of 1° and a 0.10 mm gap. Data of viscosity and normal stress versus shear rate are shown in Figure 3.5 for all the fluids used.

All non-Newtonian fluids exhibited shear-thinning with different rheological indices and elasticity. The PA solution showed elastic effects that could be negligible at shear rates higher than 500, therefore, it was considered as inelastic non-Newtonian fluid. The best fit was obtained using the Cross model. Table 3.1 shows the rheological parameters of the model for the fluids investigated.

Fluid	η_0 [Pa·s]	C [s]	m
PA	0.2451	0.06973	0.6163
CMC	2.141	0.05707	0.6246
CMC-PG	19.46	1.325	0.598

Table 3.1. Constants for the Cross model for the solutions.

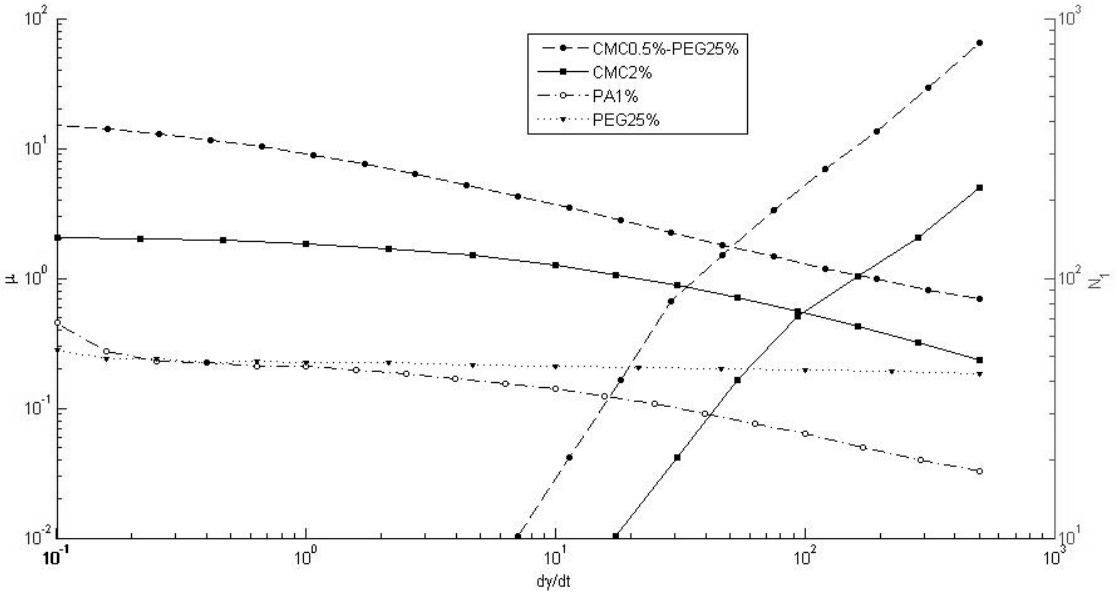

Figure 3.5. Viscosity and first Normal Stress Difference for the solutions.

3.5. Image processing

Numerical data obtained with the PIV visualizations were processed with the MATLAB software to obtain the streamlines, vorticity maps, plots, etc. Fortran and Tecplot were first considered as images processing software, however, MATLAB offered the possibility of actualise immediately each time once a change in the code is made. Due to the relatively high contraction ratio, it was necessary to take (at least) two different experiments with a different time between photos in each one and then joined together to obtain the whole field. This was made because for the high velocity zones, visualization with higher time between photos did not allow to obtain velocity maps and in the low velocity zones, visualizations with lower time between photos gave velocities lower than the actual.

Numerical data was filtered to eliminate trash data in the parabolic contraction with a mask created with the MATLAB software.

4. Results

4.1. Measurement validation

Figure 4.1 shows the velocity profiles for fully developed Newtonian flow at a distance far enough of the contraction ($z \approx 45$ [mm]) compared with the corresponding theoretical velocity profile of flow through a pipe (Hagen-Poiseuille equation). At the centre, the primary source of inaccuracies was the presence of bubbles which were formed in the fluid and dragged in it, principally, at high volumetric flows; meanwhile, for the near-wall zone, low resolution related with the PIV technique and distortion due to the curvature of the pipe gave an underestimation of the axial velocity. In spite of those troubles, good agreement was found between the theoretical and experimental results for Newtonian fluids. This agreement varied depending on the volumetric flow and the axial position.

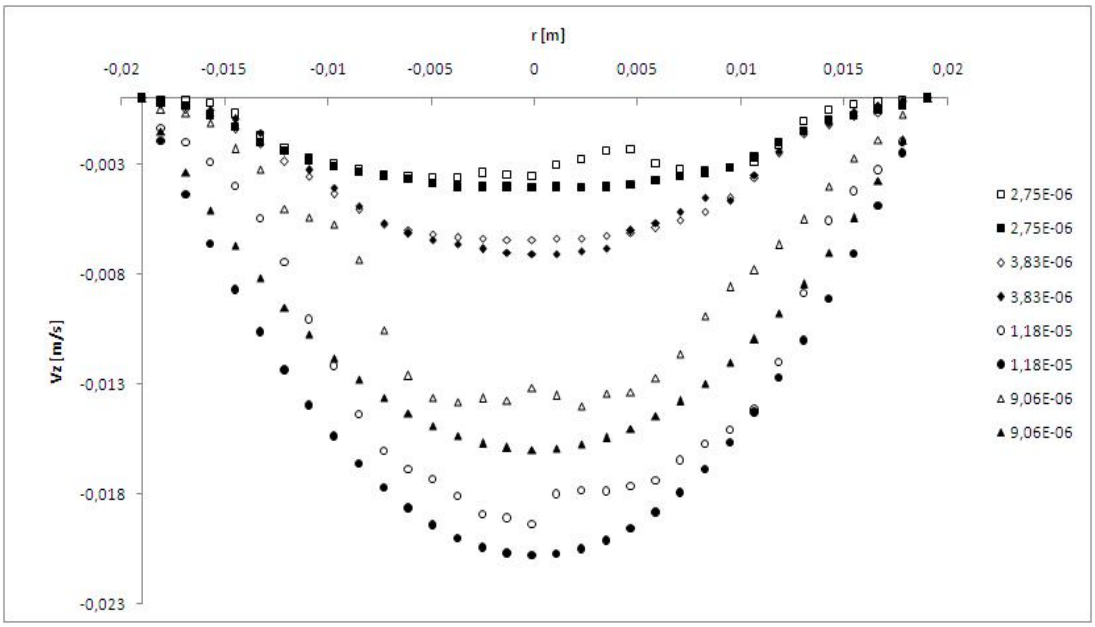

Figure 4.1. Theoretical and experimental axial velocity profile for Newtonian flow for diverse volumetric flows rates (m^3/s). Open symbols corresponding to experimental data and filled symbols corresponding to the theoretical ones.

An underestimation of the volumetric flow rate respect to the experimentally measured one was observed because of the same reasons given in the last paragraph but even with that, relatively good agreement was noticed (Figure 4.2) for the Newtonian flow through the abrupt contraction. Besides, the volumetric flow rates were manually measured (test tube and chronometer), thus little errors were expected. In general, differences between 10% and 30 % were found between the calculated and the measured volumetric flow rates for the abrupt contraction. Something quite similar was observed for the parabolic contraction as can be seen in Figure 4.3. Therefore, the results obtained can be taken as valid considering the relatively good agreement for the Newtonian data.

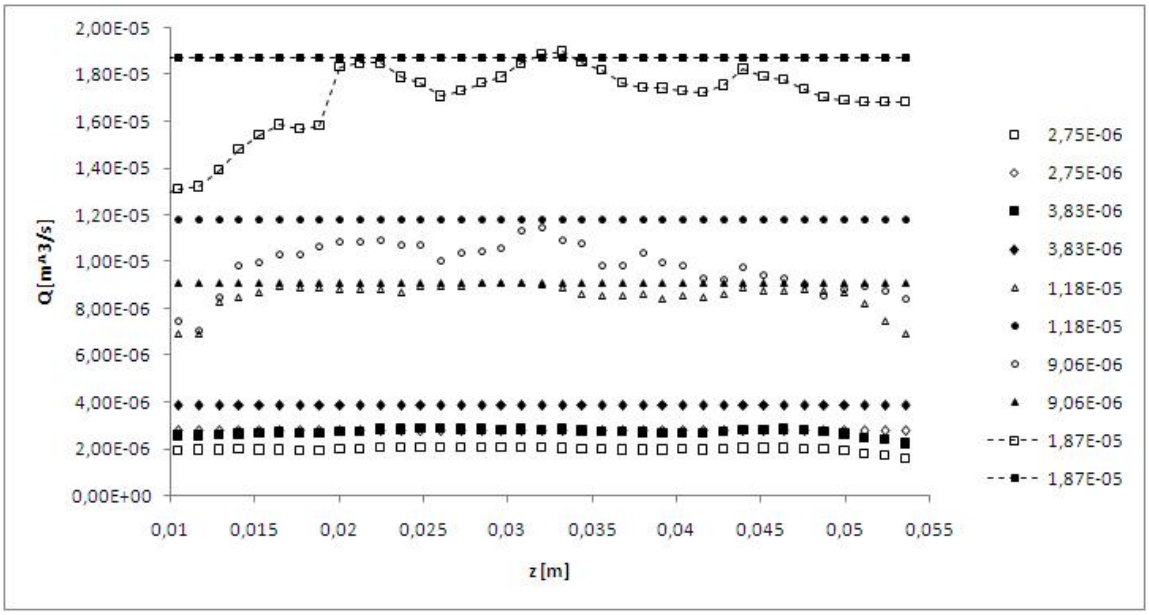

Figure 4.2. Volumetric flow rate as a function of the axial position for the PG 25% solution through the abrupt contraction. Open symbols corresponding to the calculated with numerical integration and close symbols the measured constant one.

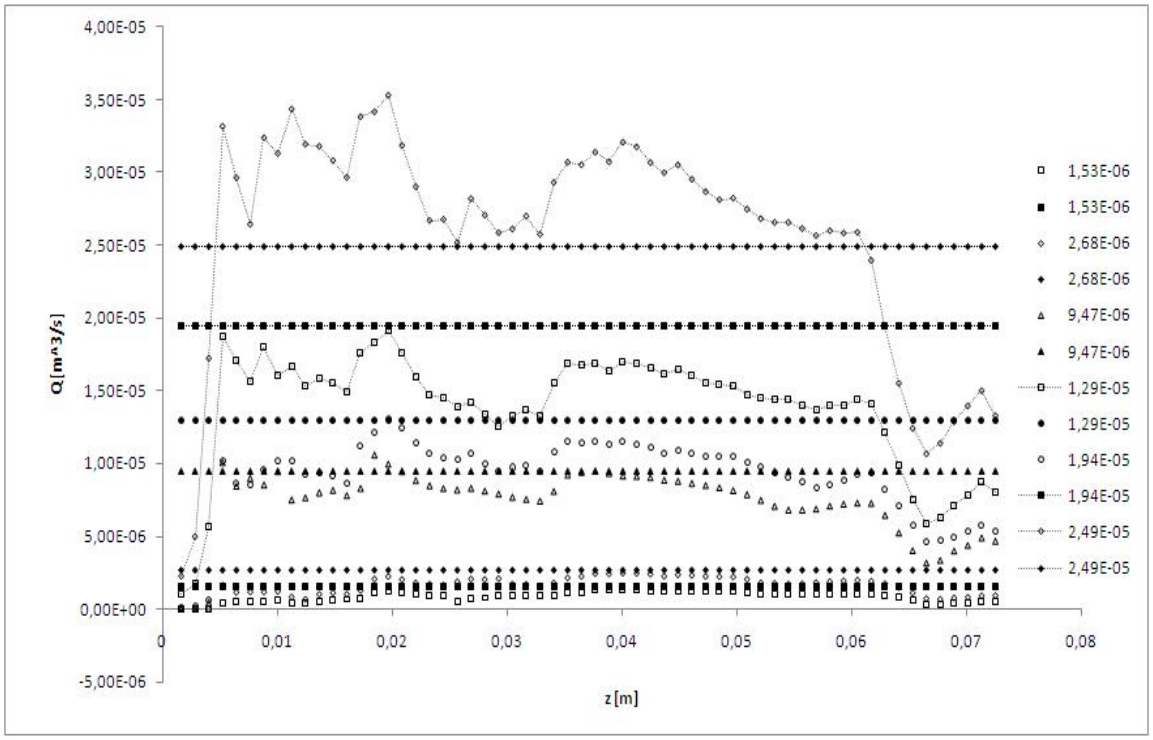

Figure 4.3. Volumetric flow rate as a function of the axial position for the PG 25% solution through the parabolic contraction. Open symbols corresponding to the calculated with numerical integration and close symbols the measured constant one.

4.2. Newtonian flow fields

Figure 4.4 and 4.5 show the vorticity (s^{-1}) and flow maps and the streamlines for several volumetric flows rates through the abrupt and the parabolic contraction respectively. For the abrupt contraction, it is observed that the streamlines tend to be pushed towards the wall of the contraction as the inertia (Reynolds number) increases in accordance with the literature; no high vortices were observed and there were stagnation zones at the corner of the contraction whose length decreased while increasing the volumetric flow rate. High-vorticity regions were noted near the walls of the pipe and in the entrance to the contraction. The last ones are consequence of the acceleration that the fluid

experiences as it flow through the contraction. A great component of shear deformation is found at the same zones also. It was also noticed that the flow was symmetric and bi-dimensional and this occurred for all the fluids and volumetric flow rates.

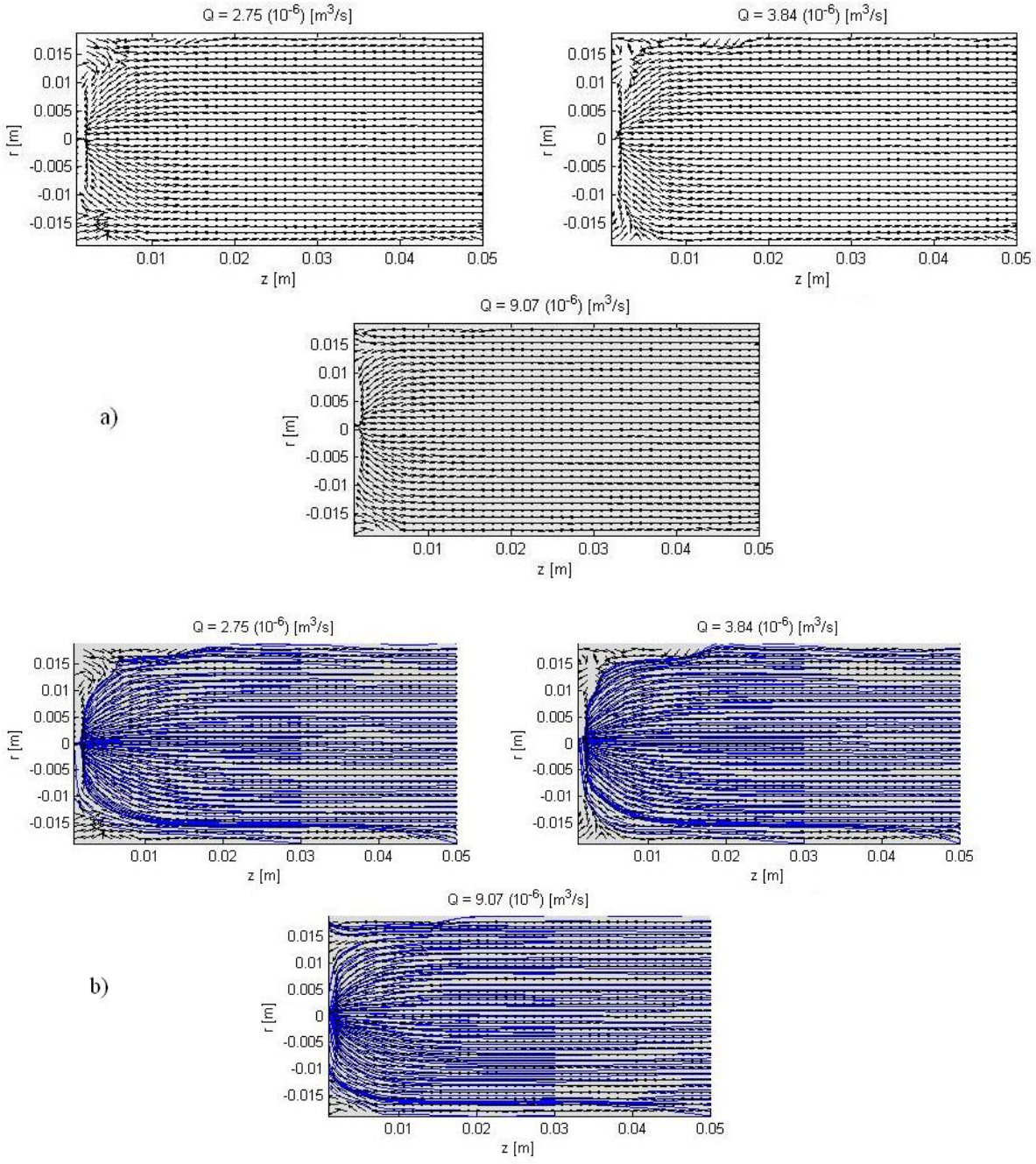

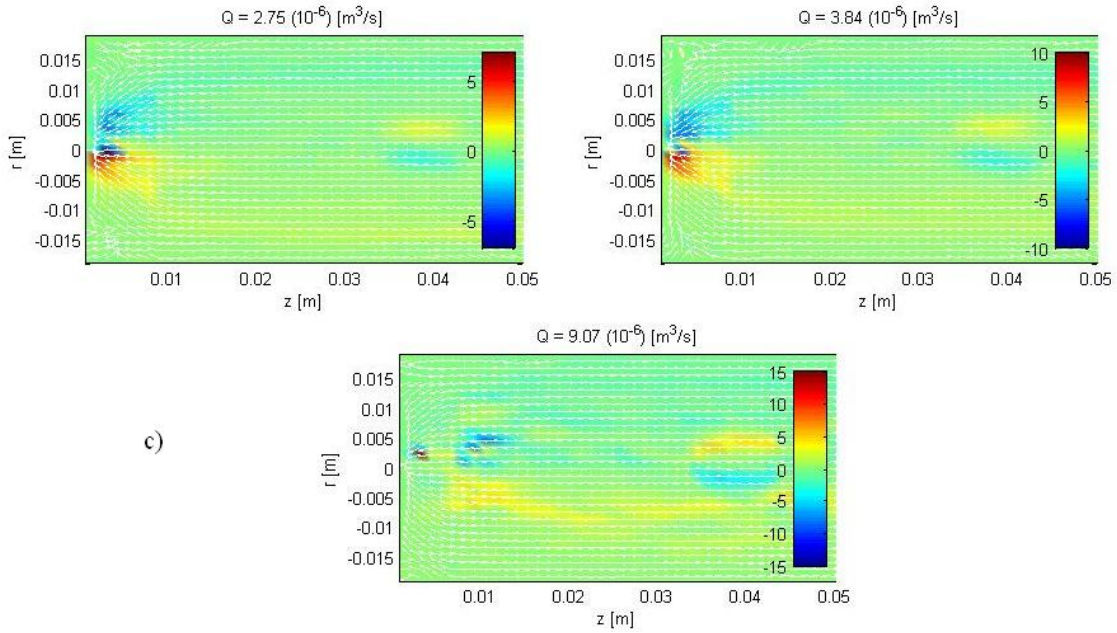

Figure 4.4. Newtonian flow fields for the abrupt contraction as a function of the volumetric flow rate: (a) Vector fields; (b) Streamlines; (c) Vorticity fields.

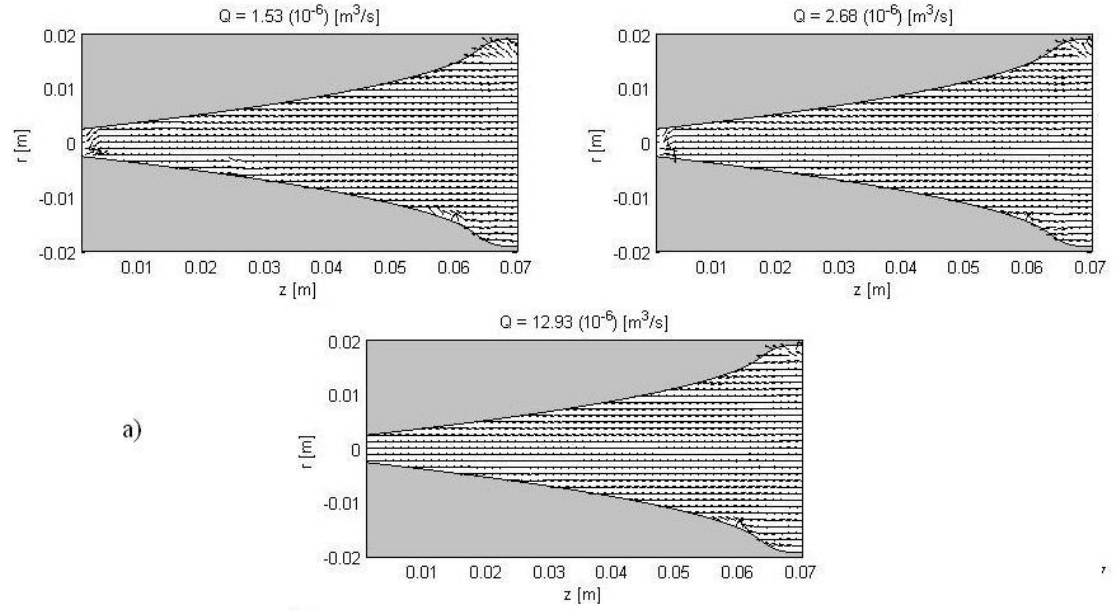

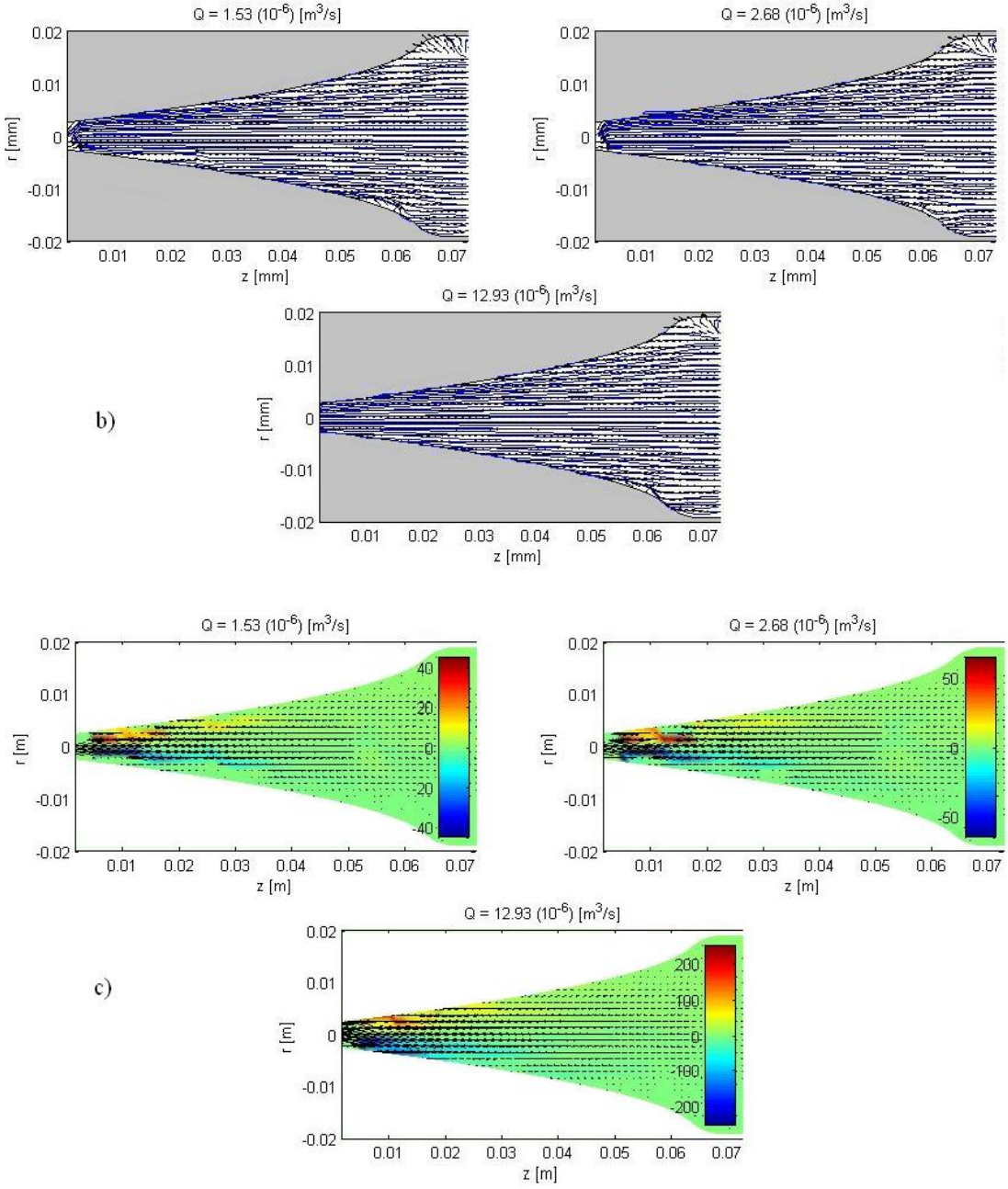

Figure 4.5. Newtonian flow fields for the parabolic contraction as a function of the volumetric flow rate: (a) Vector fields; (b) Streamlines; (c) Vorticity fields.

For the case of the parabolic contraction, a free-vorticity nucleon is observed with high vorticity components near the wall only at the thinnest part of the contraction. Neither

secondary flows nor stagnation points were observed. Thus, recalling Eq. (29), Eq. (33) and Eq. (34)

$$\left(-\frac{dR}{dz}\right) \geq \left(-\frac{dR}{dz}\right)_{contraction}$$

$$\left(\frac{dR}{dz}\right)^{t+1} = \frac{k(n+1)^{t+1}}{lt(3n+1)n^n I_{nt}}\left[\frac{(3n+1)Q}{\pi R^3}\right]^{n-t},$$

$$I_{nt} = \int_0^1 \left\{ abs\left[2 - \left(\frac{3n+1}{n}\right)\phi^{1+1/n}\right]^{t+1} \phi d\phi \right\}$$

$$\left(\frac{dR}{dz}\right)_{contraction} = \begin{cases} \dfrac{1}{0.46664(19-R)}, \cdots 0 \leq z \leq 63.3921 \\ \dfrac{68.6656 - z}{R - 11.5}, \cdots 63.3921 < z \leq 68.6656 \end{cases}$$

Considering Newtonian fluid ($n = t = 1$, $3\mu = k$, $l = \mu$) and calculating Eq. 33 we obtain

$$\frac{dR}{dz} = -1/\sqrt{2},$$

being this result independent of the volumetric flow. Hence, for the parabolic part, after doing some algebra, to avoid the separation of the streamlines from the wall, the following has to occur,

$$\begin{aligned} R &< 19 + \sqrt{2}/0{,}46664 \\ z &> 68.6656 + 7.5/\sqrt{3} \end{aligned},$$

for the parabolic contraction. This result would suggest no flow separations, as it was experimentally observed, at the parabolic part of the contraction. However, for the part of the radius where the parabola unites the wall, the algebra would suggest the opposite, which was not experimentally observed (Figure 4.6).

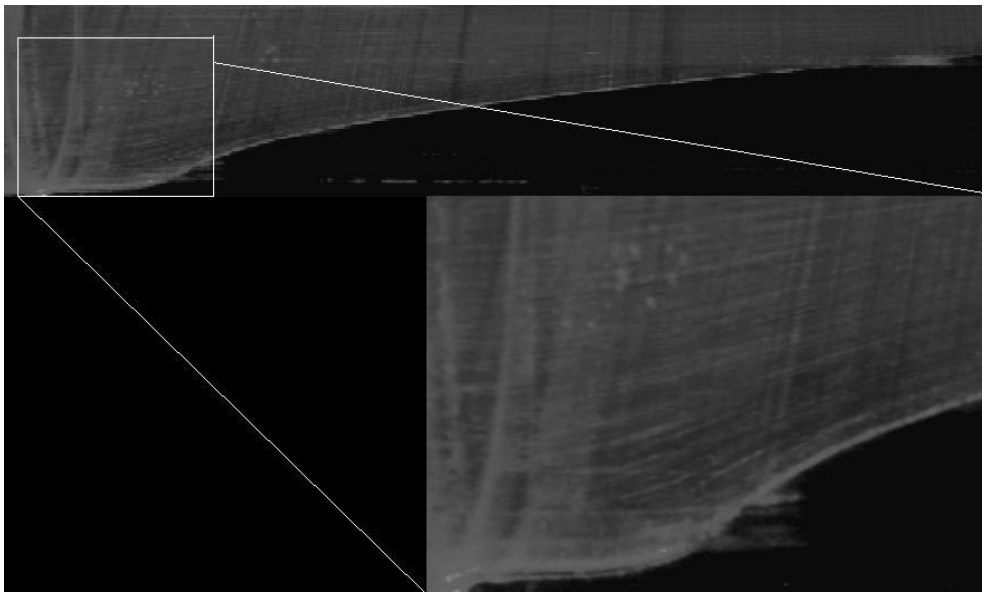

Figure 4.6. Streamlines for Newtonian Flow through the parabolic contraction (Streakline photography).

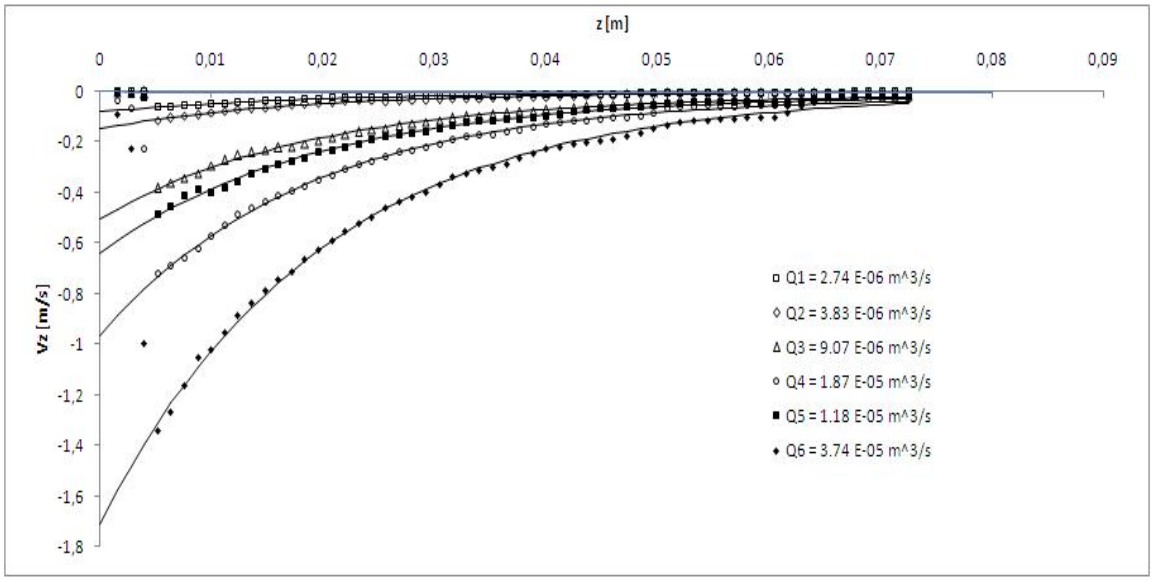

Figure 4.7. Axial velocity at the centre of the parabolic contraction for the PG solution.

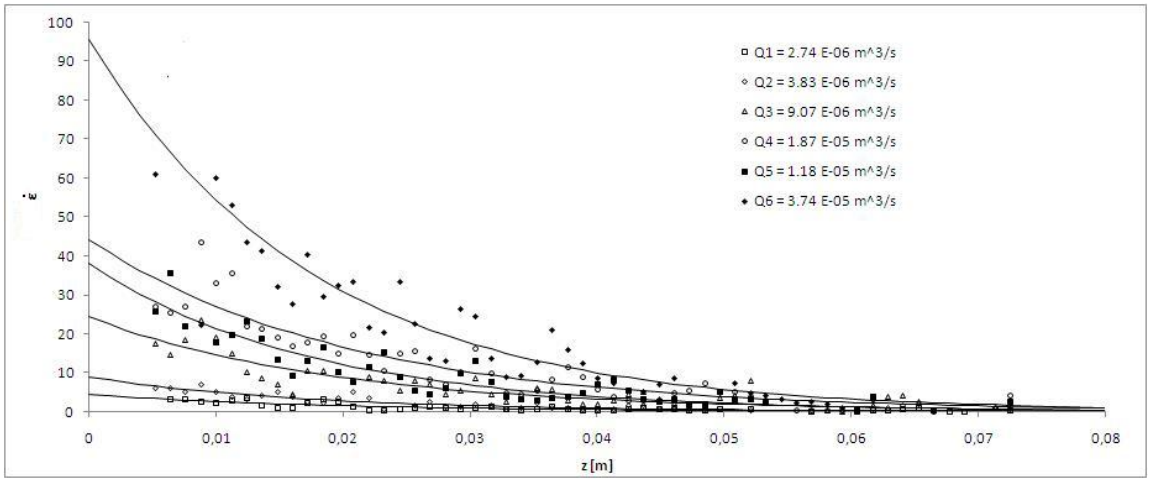

Figure 4.8. Elongational deformation rate at the centre of the parabolic contraction for the PG solution.

Figures 4.7 and 4.8 show the axial velocity and the elongational deformation rate at the centreline along the contraction. Axial centre velocity was found to exponentially increase starting at the beginning of the contraction ($z \approx 68$ [mm]) and the elongational deformation exhibited a similar behaviour. Upstream, fully developed profiles were noticed (constant *Vz* and $\dot{\varepsilon}=0$). Figure 4.9 shows the dimensionless axial velocity profile with the Newtonian fluid. A fairly good agreement is found between the experimental results and profile theoretically obtained for Newtonian flow for the dimensionless axial velocity as a function of the dimensionless radius. Nevertheless, relatively big differences are observed in the regions $-1 < r^* < -0.5$ and $0.5 > r^* > 1$, which are consequences of marks generated during the manufacturing of the contraction.

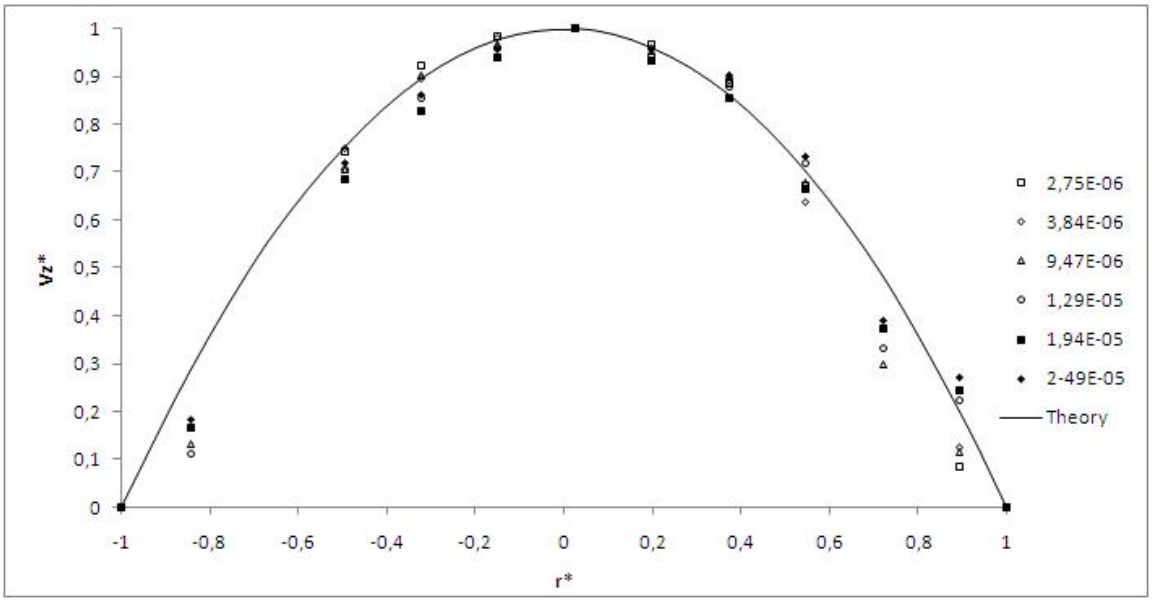

Figure 4.9. Experimental dimensionless axial velocity profile compared with the theoretical one.

4.3. Inelastic Non-Newtonian flow fields

Figure 4.10 and 4.11 show the flow fields for the abrupt contraction and the parabolic contraction with the PA solution. The streamlines were pushed towards the contraction and converge to the abrupt contraction as the volumetric flow rate increases, something similar to the Newtonian flow. In this case, no presence of divergent flow is noticed as a result of the absence of normal stresses, which is in good agreement with the findings reported by Alves and Poole (2007). Higher values of vorticity near the walls are found at higher volumetric flows as well as a nucleon with relatively low values of vorticity indicating zones with relative low shear deformation. The similar behaviour between the PG and the PA solution confirmed that the elasticity is the principal factor to the vortices appears.

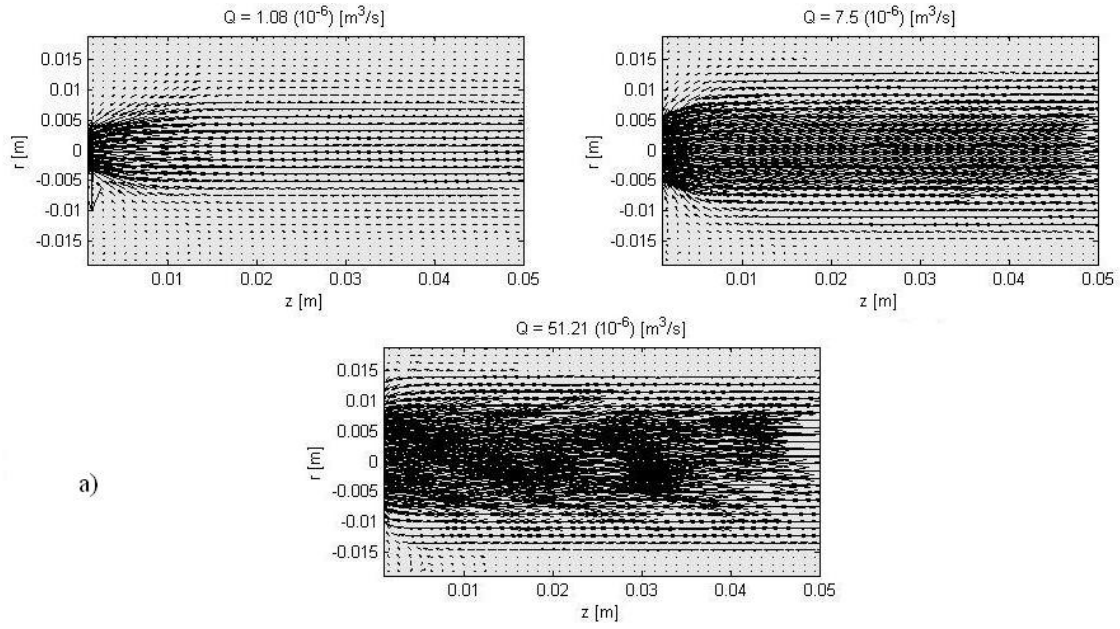
Q = 1.08 (10-6) [m3/s]
Q = 7.5 (10-6) [m3/s]
Q = 51.21 (10-6) [m3/s]
r [m]
z [m]
0.015
0.01
0.005
0
-0.005
-0.01
-0.015
0.01
0.02
0.03
0.04
0.05

a)

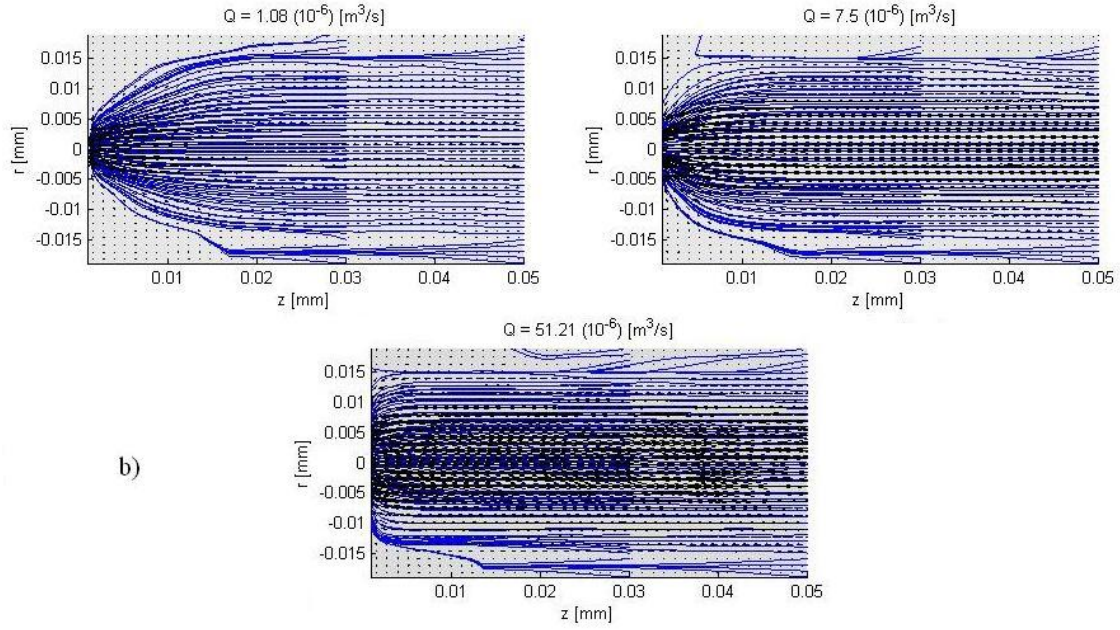
Q = 1.08 (10-6) [m3/s]
Q = 7.5 (10-6) [m3/s]
Q = 51.21 (10-6) [m3/s]
r [mm]
z [mm]
0.015
0.01
0.005
0
-0.005
-0.01
-0.015
0.01
0.02
0.03
0.04
0.05

b)

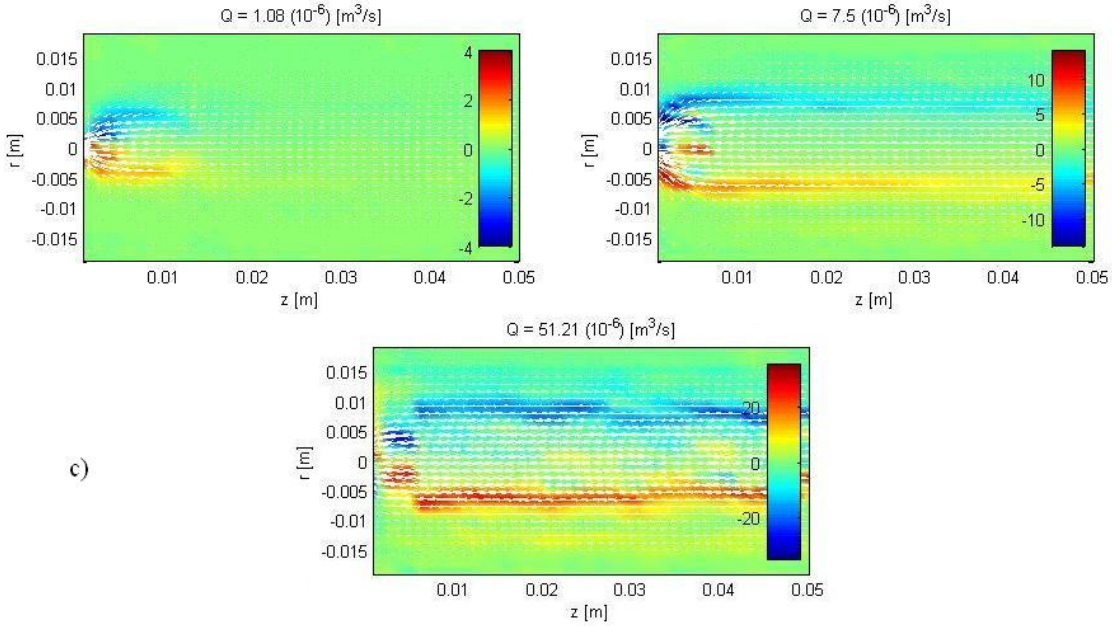

Figure 4.10. PA flow fields for the abrupt contraction as a function of the volumetric flow rate: (a) Vector fields; (b) Streamlines; (c) Vorticity fields.

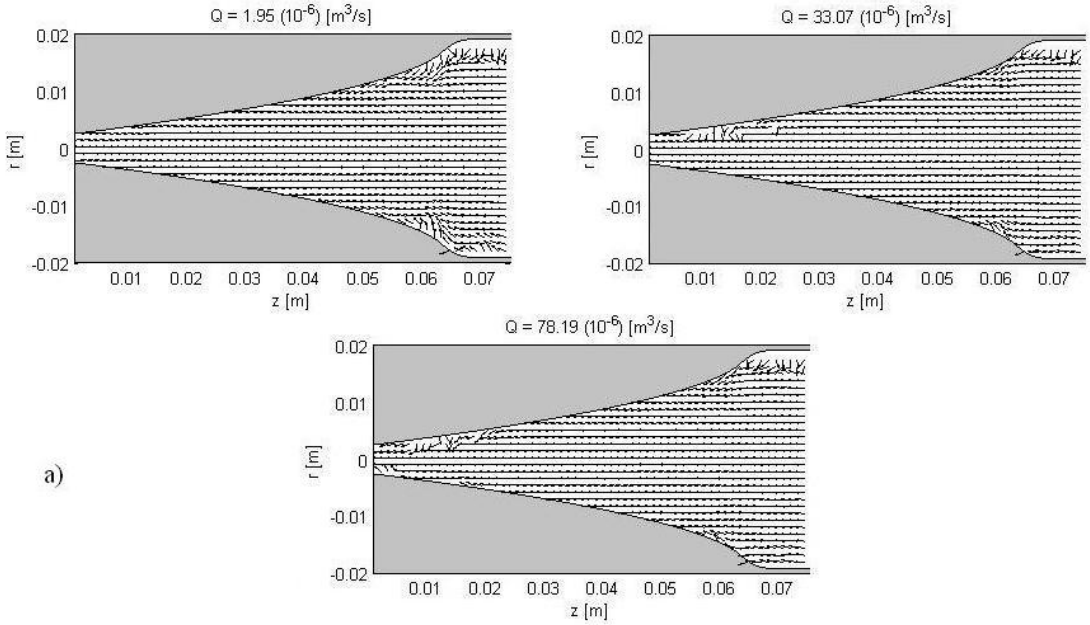

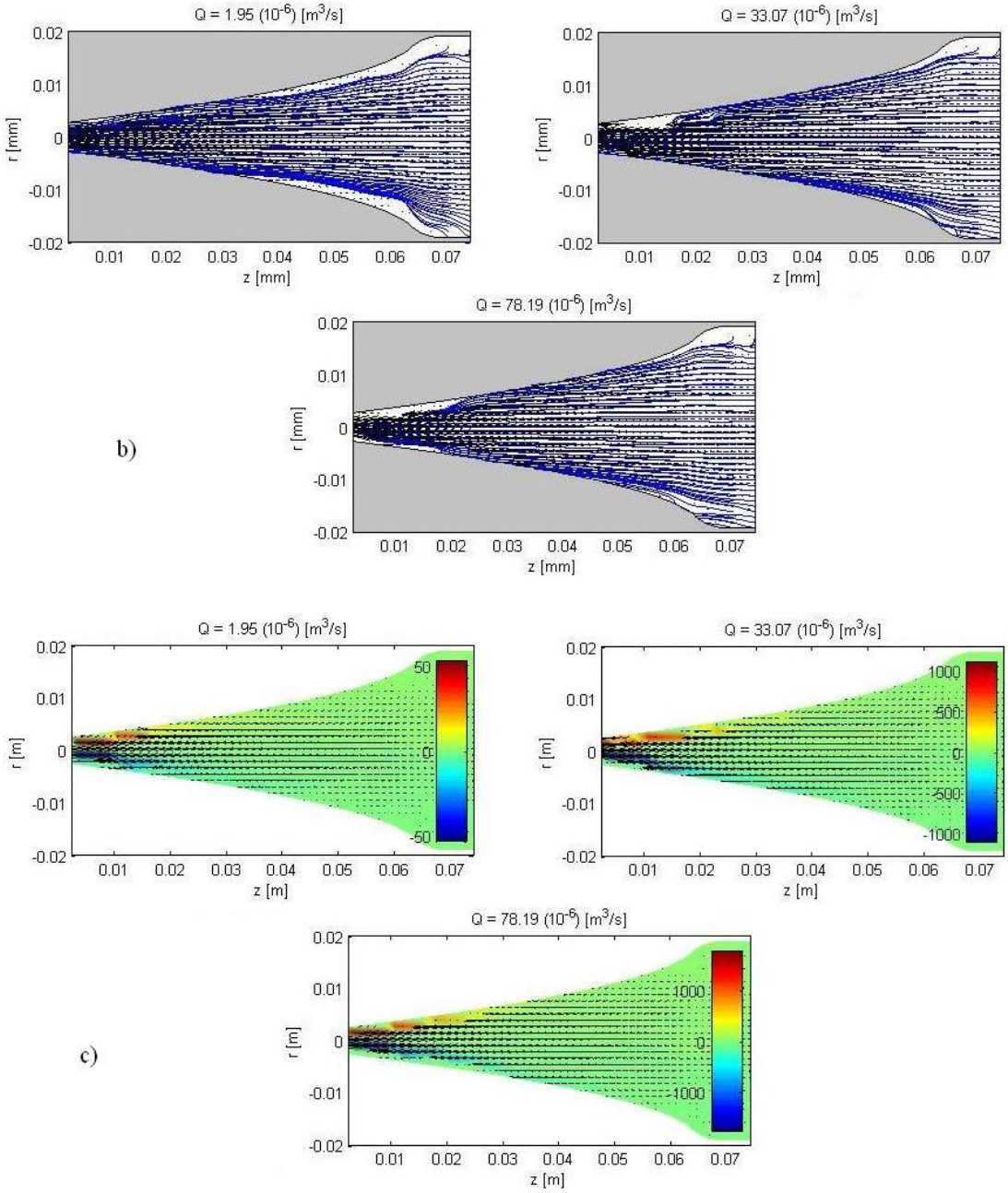

Figure 4.11. PA flow fields for the abrupt contraction as a function of the volumetric flow rate: (a) Vector fields; (b) Streamlines; (c) Vorticity fields.

For the parabolic contraction, there are higher vorticity zones in the contraction's neck with an almost free vorticity nucleon in a quite similar way to the Newtonian case. In both,

secondary flow and streamlines separation were not observed. As reported in the literature, flow separation is commonly a consequence of elastic effects, hence, it was expected that it didn't appear in the PA flow.

4.4. Elastic non-Newtonian flow fields

Figure 4.12 shows a snapshot of the flow for the CMC solution through the abrupt contraction were the vortices can be clearly observed as a consequence of the elastic effects. Figures 4.13 and 4.14 show the flow fields in terms of vector fields, streamlines and the vorticity (s^{-1}) as a function of the volumetric flow rate for the abrupt and parabolic contractions, respectively, with the same CMC solution.

For the abrupt contraction, the vortices length increased while increasing the volumetric flow rate; nonetheless, the vortices length tends to decrease if the volumetric flow further increased. An explanation of this behaviour could be than first, as increasing the volumetric flow rate (and the shear rate), the elastic forces increased and dominated, thus, the vortices length tended to increase in magnitude; thereafter, if the elasticity of the fluid is not so high, while increasing the volumetric flow rate, the inertial effects tended to dominate the elastic effects and the vortices length decreased. Relatively high vorticity zones were found near the contraction were the flow converges and interacts with the vortices.

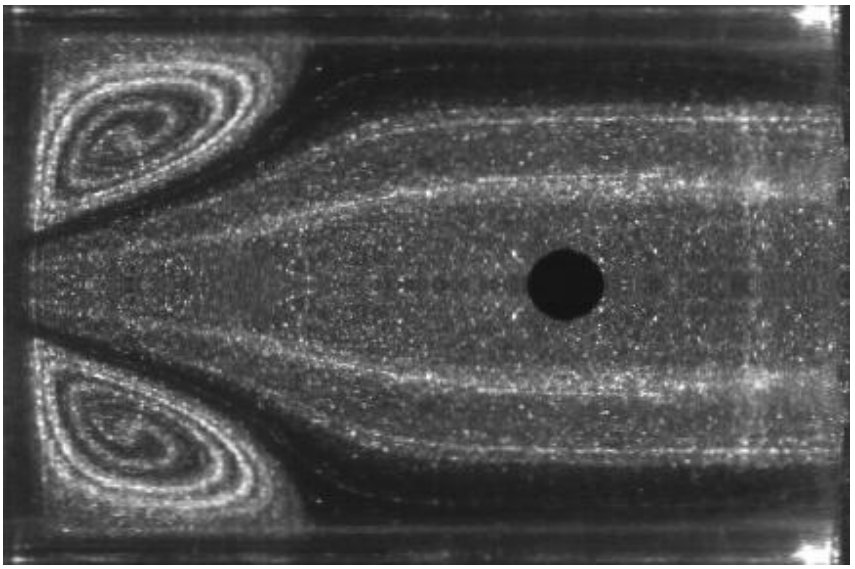

Figure 4.12. Vortices in the flow of the CMC solution through the abrupt contraction.

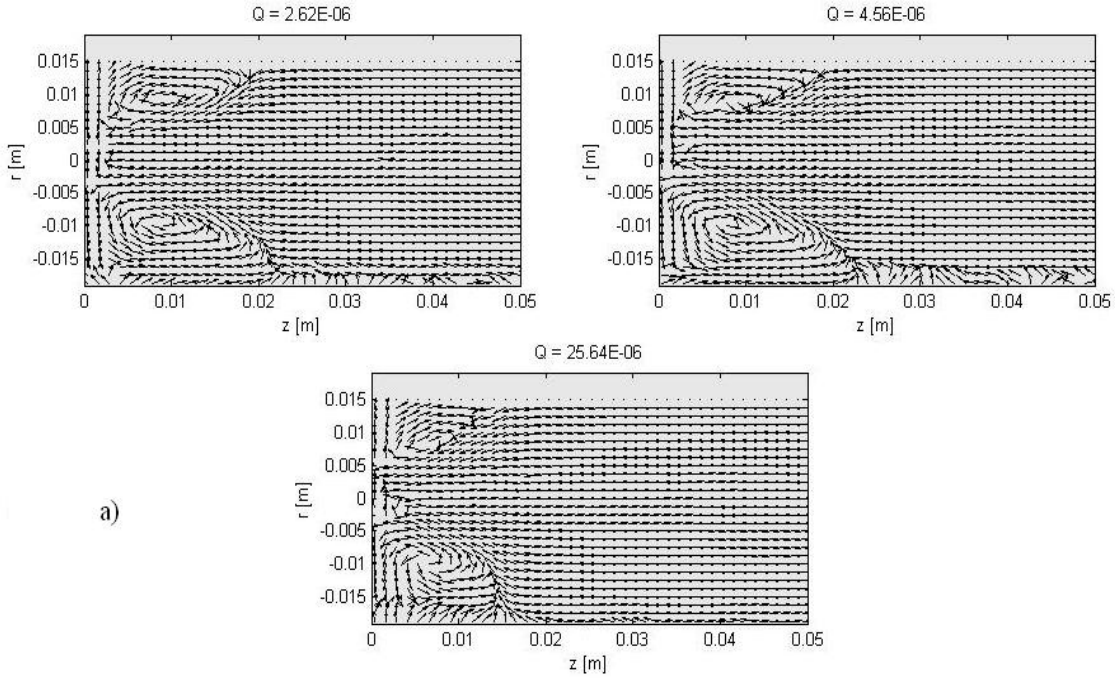

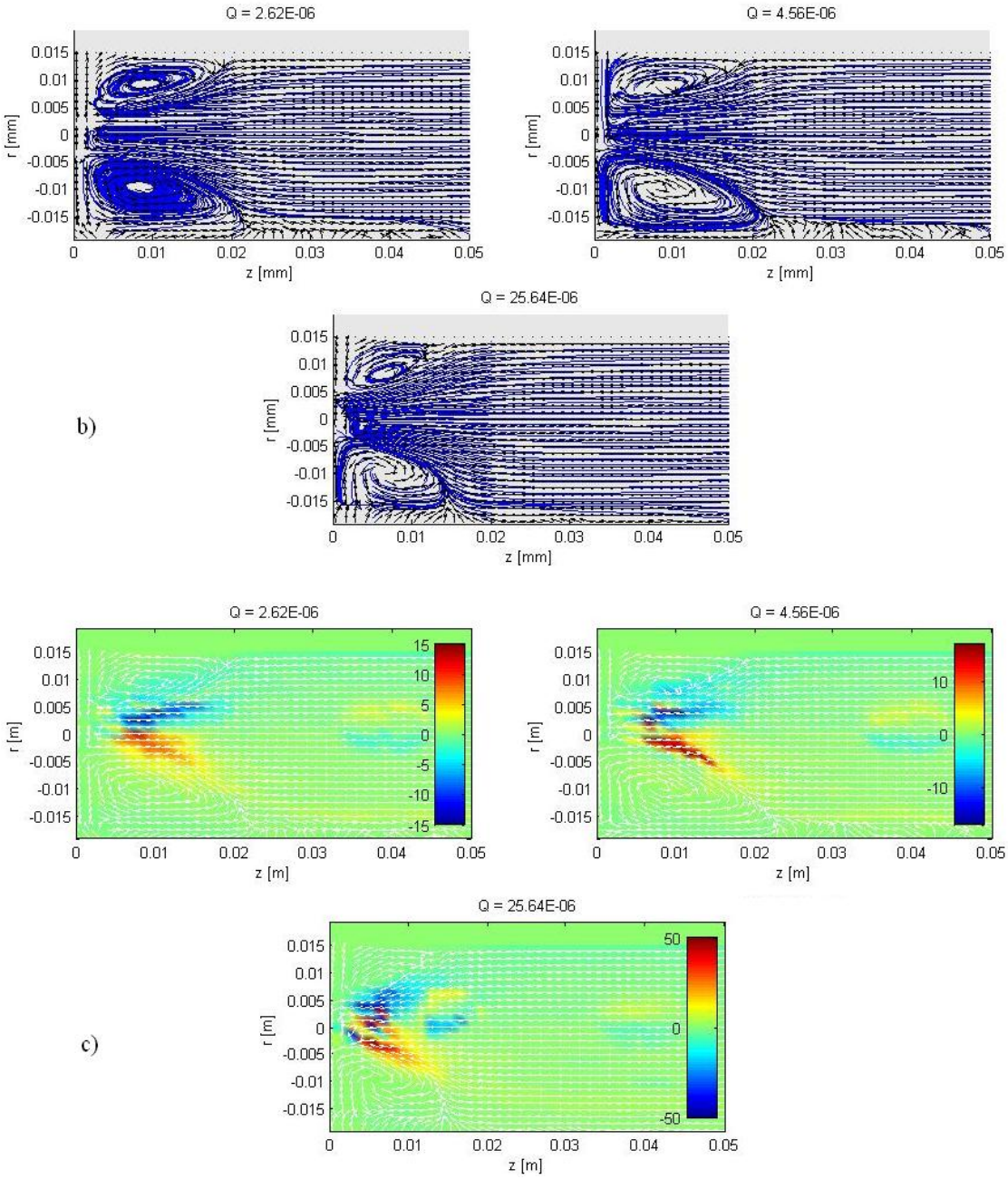

Figure 4.13. CMC flow fields for the abrupt contraction as a function of the volumetric flow rate: (a) Vector fields; (b) Streamlines; (c) Vorticity fields.

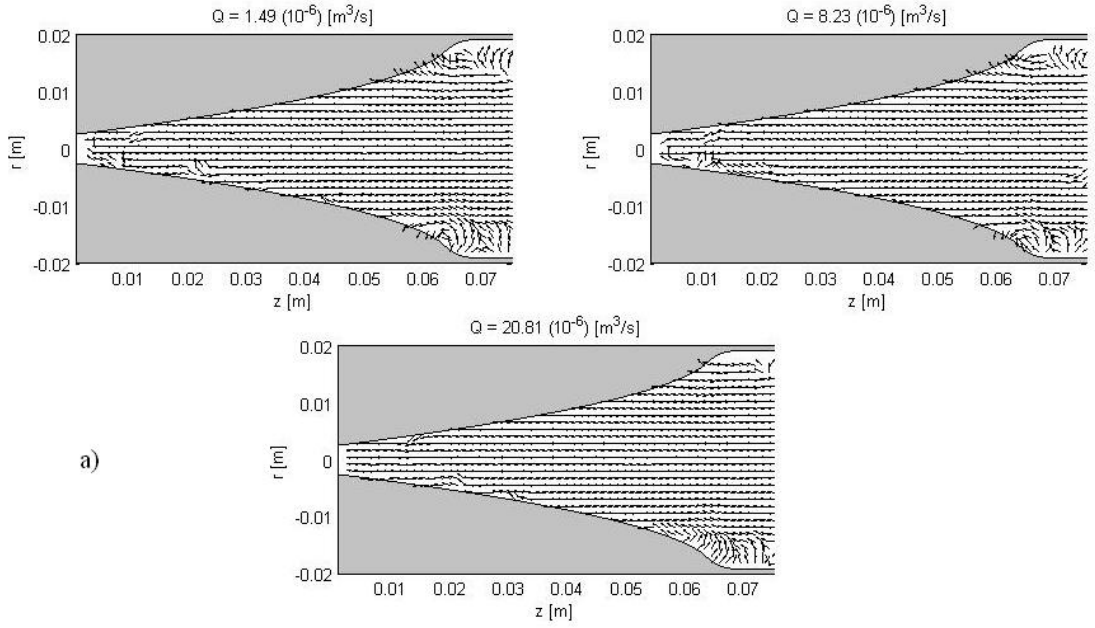
Q = 1.49 (10-6) [m3/s]
Q = 8.23 (10-6) [m3/s]
Q = 20.81 (10-6) [m3/s]
r [m]
z [m]
0.02
0.01
0
-0.01
-0.02
0.01 0.02 0.03 0.04 0.05 0.06 0.07

a)

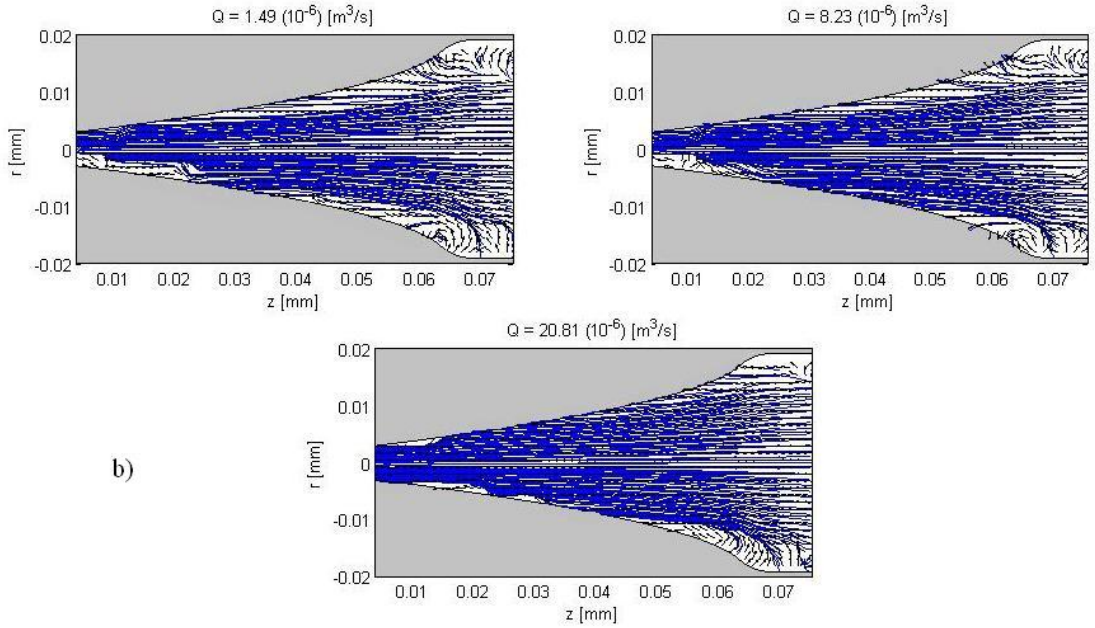
Q = 1.49 (10-6) [m3/s]
Q = 8.23 (10-6) [m3/s]
Q = 20.81 (10-6) [m3/s]
r [mm]
z [mm]
0.02
0.01
0
-0.01
-0.02
0.01 0.02 0.03 0.04 0.05 0.06 0.07

b)

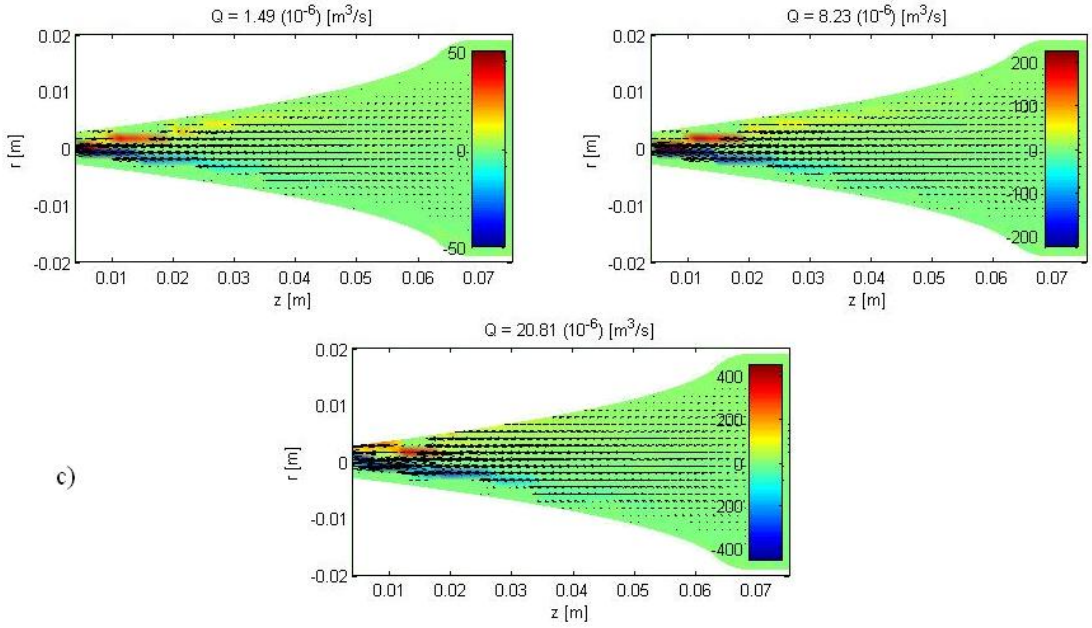

Figure 4.14. CMC flow fields for the parabolic contraction as a function of the volumetric flow rate: (a) Vector fields; (b) Streamlines; (c) Vorticity fields.

For the parabolic contraction, despite the streamlines obtained with the PIV numerical data separate from the walls, no secondary flow is noticed. High vorticity zone with high-shear deformation were found at the thinnest part of the contraction and an almost-free vorticity nucleon was noticed also. Apparently, the behaviour did not largely vary respect to the inelastic fluids. A second snapshot was taken to observe the behaviour far beyond the beginning of the contraction and to prove that, effectively, there was no secondary flow. Results can be seen in Figure 4.15. Nevertheless, because of the surface roughness generated by the manufacturing process, the resolution of the PIV technique in the beginning of the contraction was not so good and numerical data do not allowed to obtain streamlines with good precision in that zone. In spite of that, it could be clearly observed that there was not secondary flow.

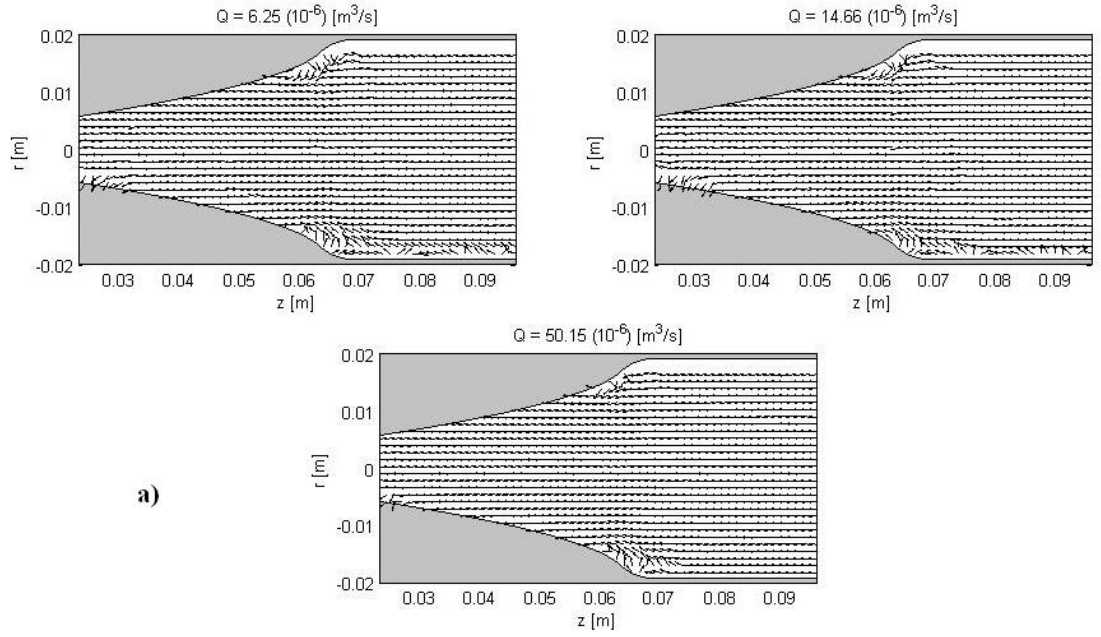
Q = 6.25 (10-6) [m3/s]
Q = 14.66 (10-6) [m3/s]
Q = 50.15 (10-6) [m3/s]
r [m]
z [m]
0.02
0.01
0
-0.01
-0.02
0.03 0.04 0.05 0.06 0.07 0.08 0.09

a)

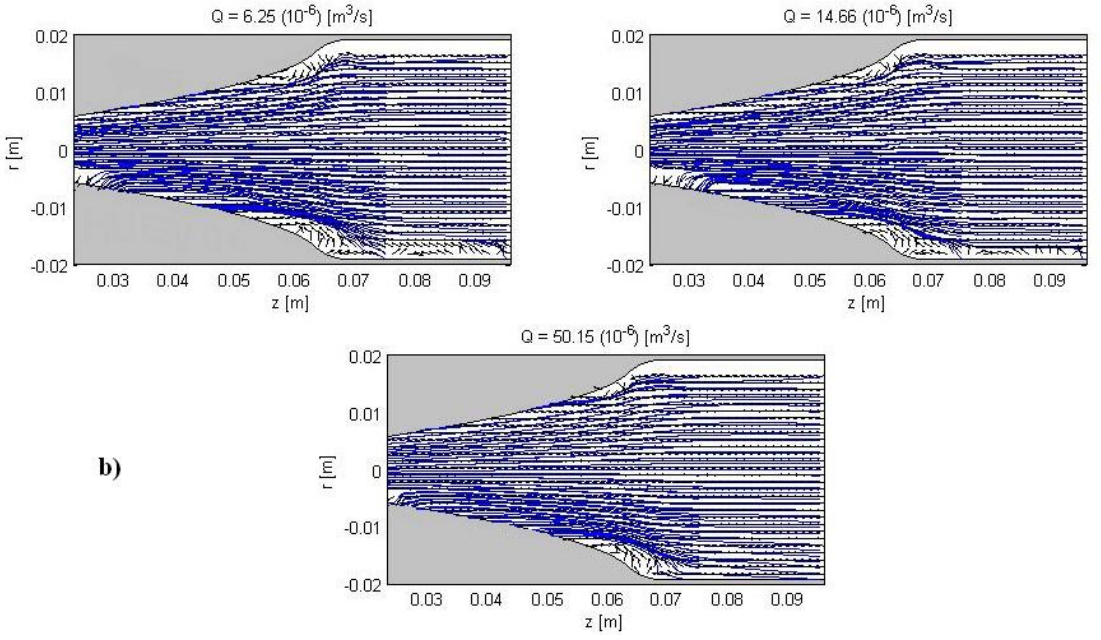
Q = 6.25 (10-6) [m3/s]
Q = 14.66 (10-6) [m3/s]
Q = 50.15 (10-6) [m3/s]
r [m]
z [m]
0.02
0.01
0
-0.01
-0.02
0.03 0.04 0.05 0.06 0.07 0.08 0.09

b)

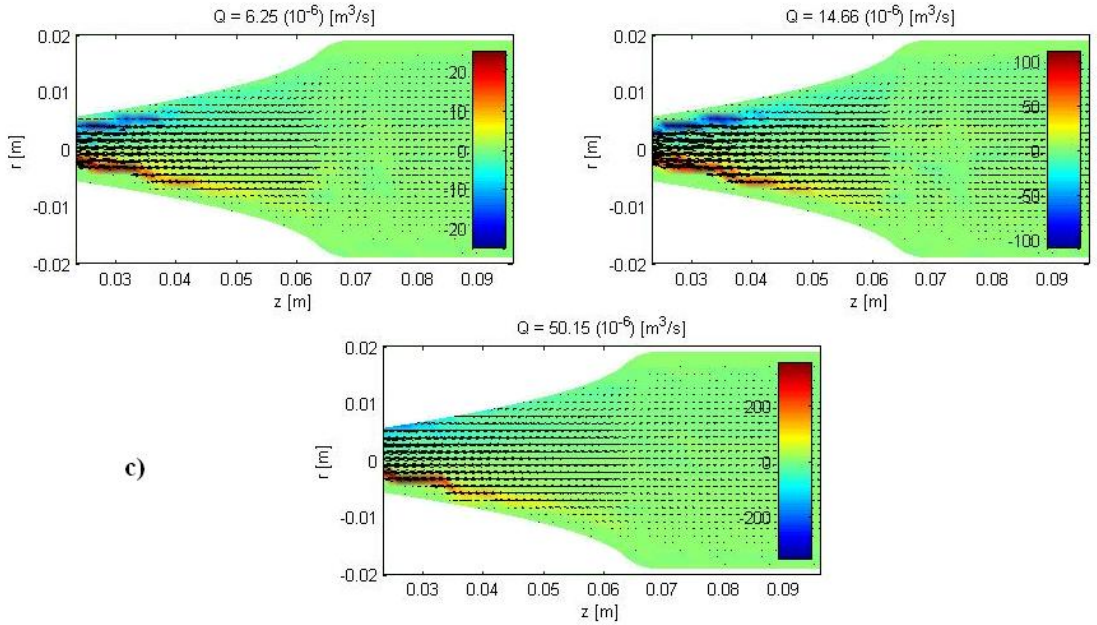

Figure 4.15. Second snapshot of the CMC flow fields for the abrupt contraction as a function of the volumetric flow rate: (a) Vector fields; (b) Streamlines; (c) Vorticity fields.

Again, it is observed a free-vorticity nucleon in almost all the region and an exponential behaviour in the axial velocity profile until reaching a plateau at z = 75 [mm] for almost all the volumetric flows and something similar occurred with the elongational deformation (Figure 4.16 and Figure 4.17). For the axial velocity as function of the radial position (Figure 4.18), the higher velocity appears in the middle of the pipe and we had no presence of "ears rabbit" or any indication of divergent flow. According with Alves and Poole (2007) and looking at Figure 4.16, divergent flow could be considered and it coincides with the part of the flow where the Trouton ratio goes to the maximum but it can be seen that the part where the axial velocity decreases, it coincides with the part of the contraction where the resolution was no so good. In addition, looking at the velocity profiles (Figure 4.18), no "rabbit ears" are observed. Also, it is important to point out that divergent flow is usually observed when using low contraction ratios, which is not the case

of the present work (RC = 8).Figure 4.18shows the dimensionless axial velocity as a function of the dimensionless radius for diverse volumetric flow rates and at different axial position in the parabolic contraction, the points for the axial velocity follow the same parabolic pattern. This could be helpful because with this, it would be possible to establish an equation to relate the volumetric flow rate to the axial centre velocity with an exponential trend.

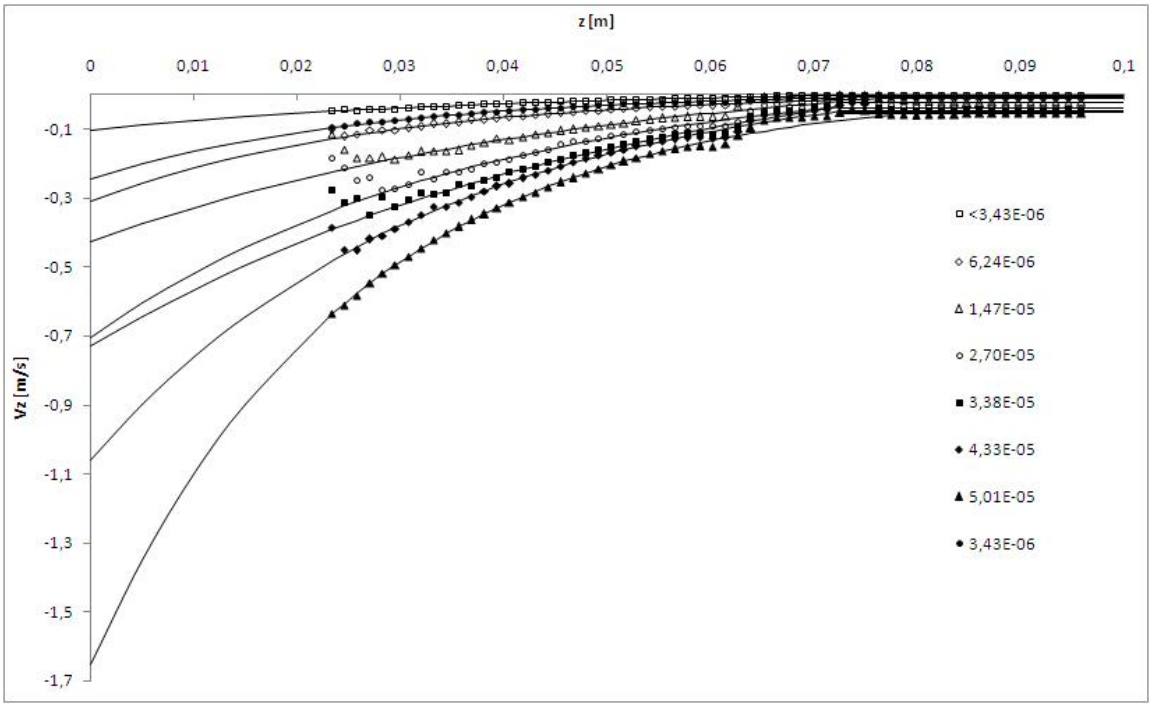

Figure 4.16. Axial velocity in the centreline for different volumetric flows for the CMC solution.

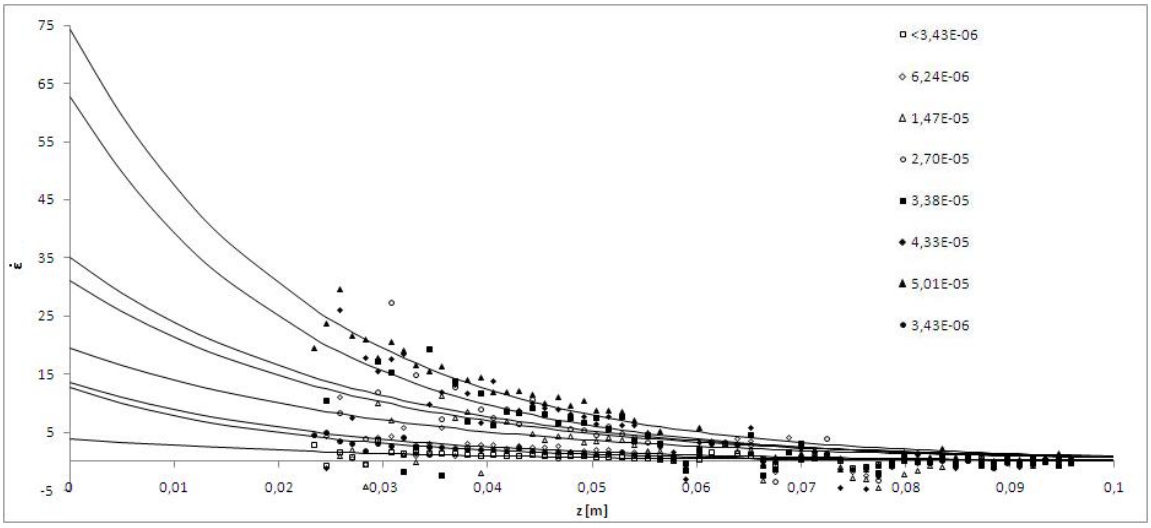

Figure 4.17. Elongational deformation rate in the centreline for different volumetric flows for the CMC solution.

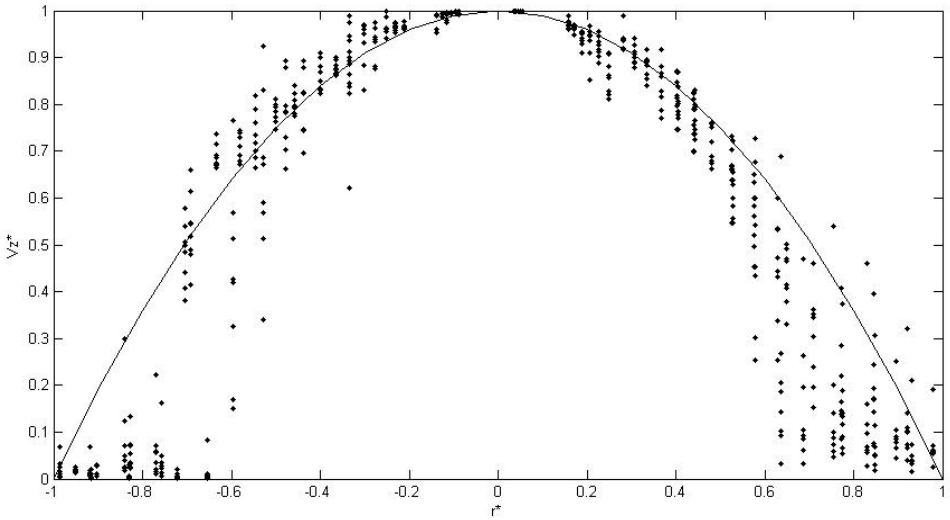

Figure 4.18. Dimensionless axial velocity at different axial positions for different volumetric flows.

Even when no vortex enhancement was observed, to be sure of that, and to see if there was flow separation, another snapshot was taken with another more elastic fluid because as we could see in the introduction, elasticity has a considerably influence in the vortex formation. To do that, the CMC-PG solution was used to take streakline photography and PIV measurements. First we show an image of the vortex for the

abrupt contraction (Figure 4.19); next, the PIV measurements made to the abrupt contraction. The highest volumetric flow was approximately 10^{-6} m^3/s and the other one could not be measured.

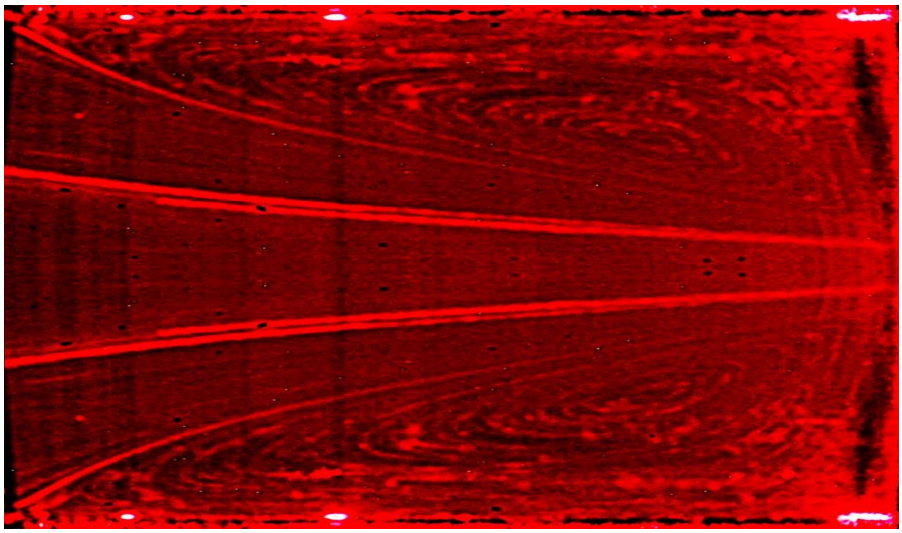

Figure 4.19. Streamlines at low volumetric flow ($Q \approx 10^{-6}$ [m^3/s]) for the CMC-PG solution. (Streakline photography).

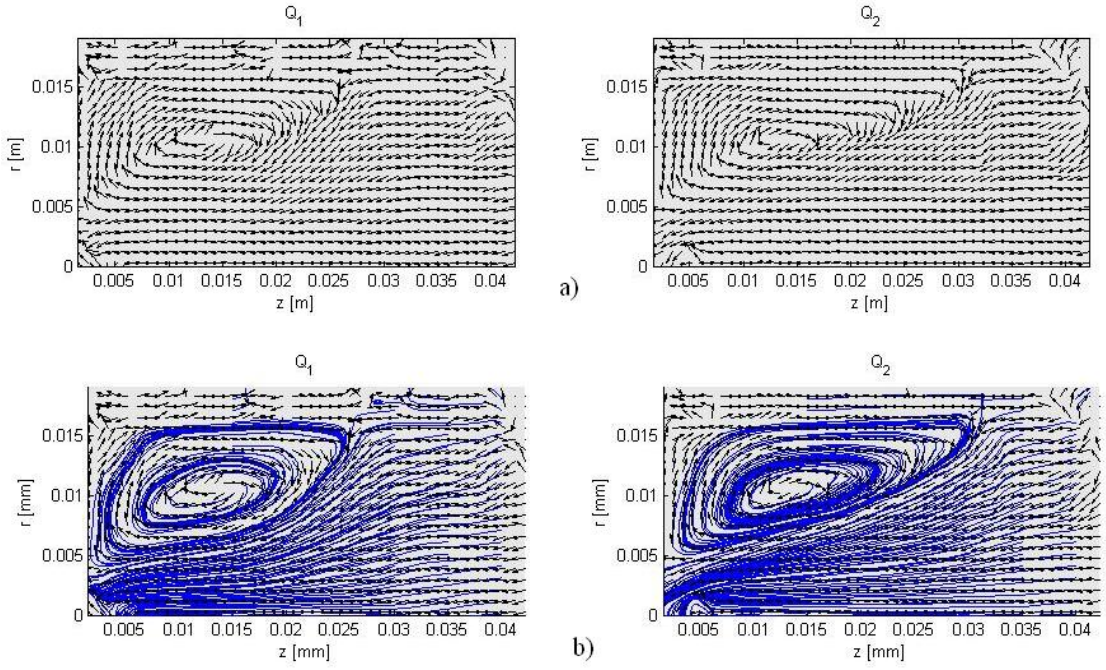

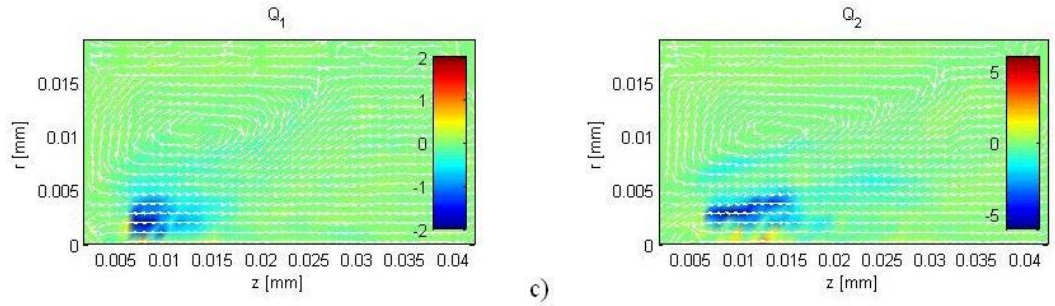

Figure 4.20. CMC-PG flow fields for the abrupt contraction as a function of the volumetric flow rate (Q_1<Q_2): (a) Vector fields; (b) Streamlines; (c) Vorticity fields.

It is observed that the vortex length increases when increasing the volumetric flow (elastic effects dominates because it is creeping flow) and again that the highest values of vorticity are in the zone where the vortices interact with the converging flow having values not so high. Now we see an image of the flow through the parabolic contraction. Presence of divergent flow in experiments was not observed one more time and a similar behaviour with the CMC solution was found. Considering low resolution near the zone where the streamlines could separate from the pipe, streakline photography was then taken. It can be seen in Figure 4.22.

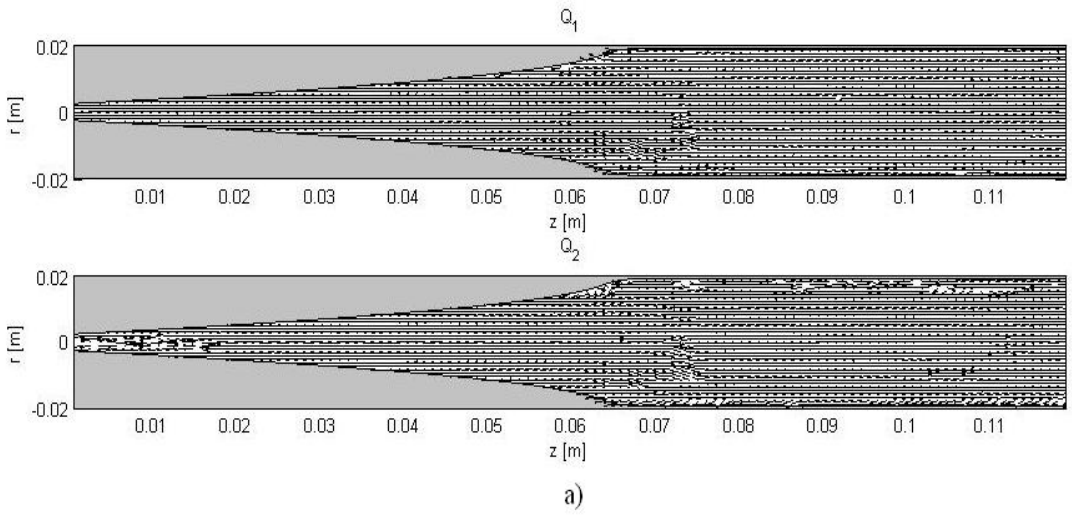

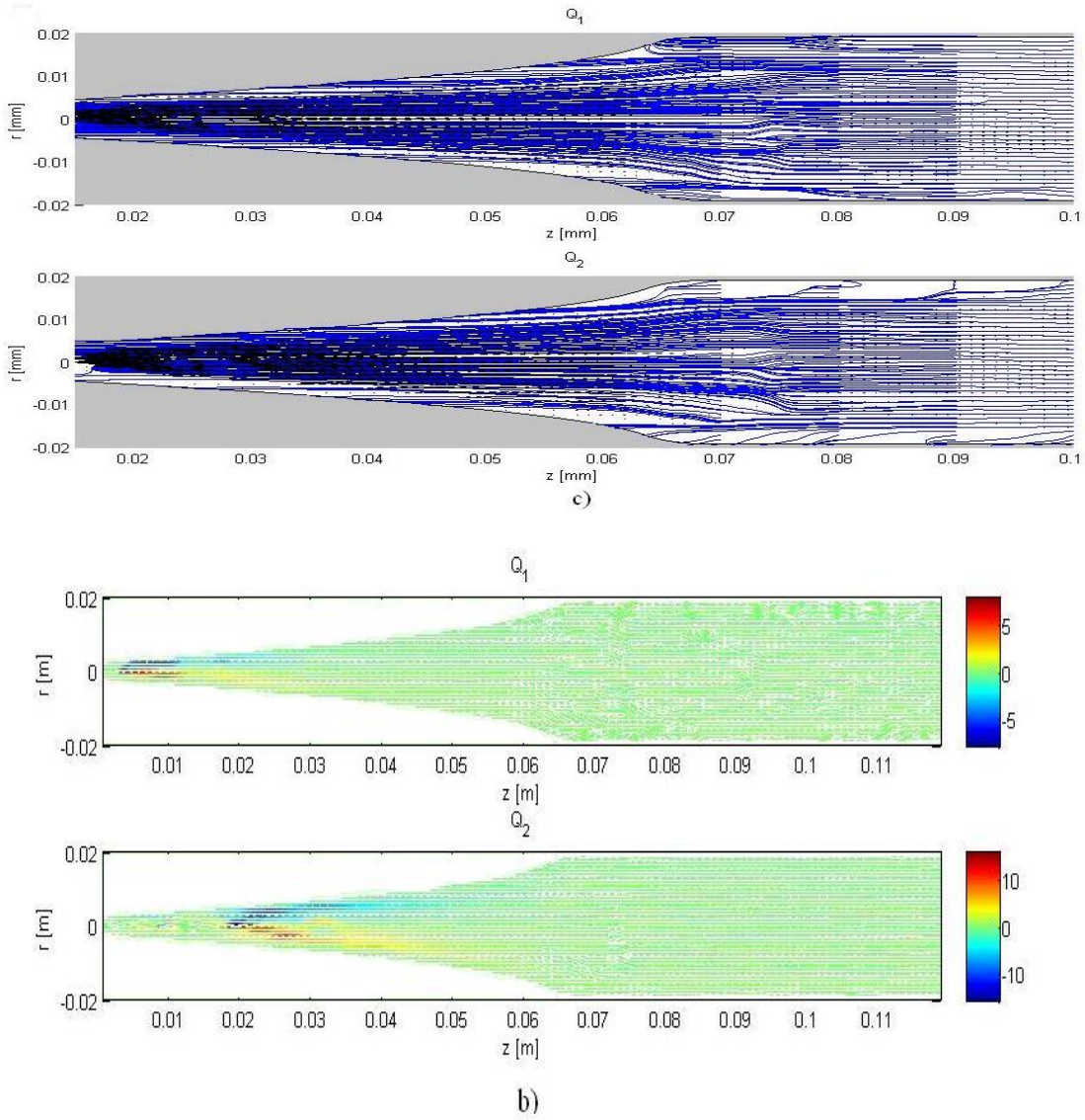

Figure 4.21. CMC-PG flow fields for the parabolic contraction as a function of the volumetric flow rate (Q_1<Q_2): (a) Streamlines; (b) Vorticity fields.

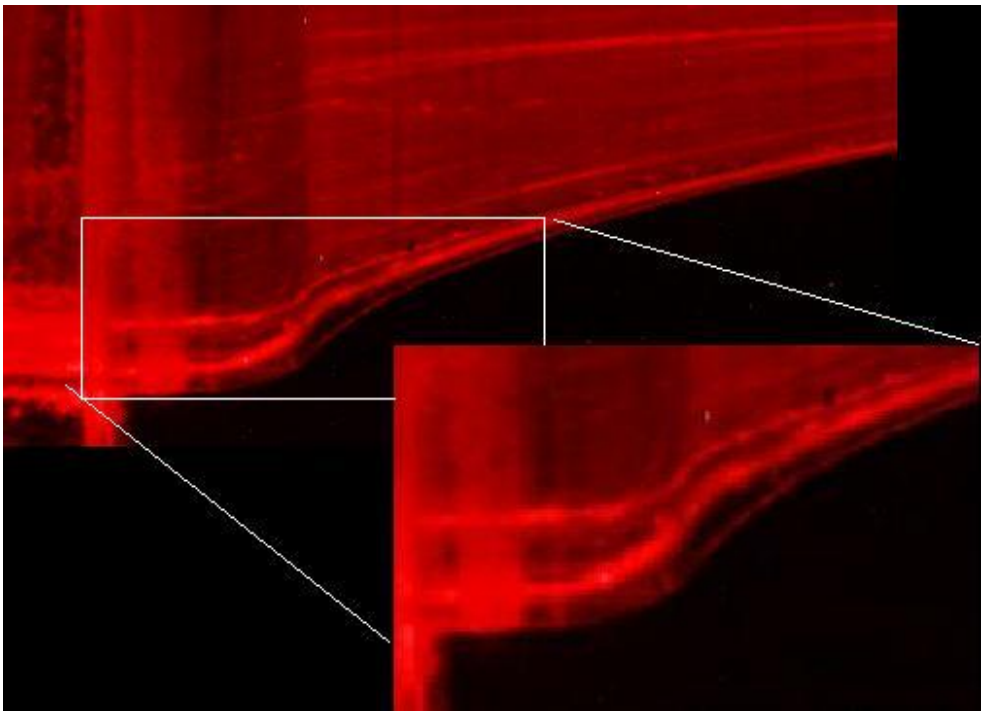

Figure. 4.22. Separation of the streamlines from the pipe at low volumetric flow rate for the CMC-PG solution through (Streakline photography).

Vortices were not observed but flow separation was noticed even at these low volumetric flow rates with the streakline photography; thus, as it was earlier mentioned, to consider two parts are needed to be considered on the Binding's analysis to calculate the extensional viscosity. That part could be computed to measure if the error is not so big because the flow separation is seen only in the beginning of the contraction; if so, then the inaccuracies could be negligible. However, flow separation occurs in presence of normal stresses in the flow and could be more visible at higher volumetric flows. Therefore, if there is separation at creeping flow, it is possible that it will be higher as the volumetric flow increases and the estimation of the extensional viscosity by using the Binding's analysis would be more inaccurate.

5. Conclusions.

The flow of Newtonian and non-Newtonian fluids through a parabolic and an abrupt contraction has been visualized. Good agreement between the theoretical and the experimental results for the Newtonian flow was found for both geometries. Additionally, in all the experiments the flow was found to be symmetric and bi-dimensional.

For the abrupt contraction, the behaviour was in good agreement with the literature: for the inelastic fluids, little stagnations and vortex zones at the corner of the contraction were observed and for the elastic fluids higher recirculation zones in the corner were noticed. For the elastic fluids, these zones first increased in length with the volumetric flow rate and eventually decreased while increasing the volumetric flow rate for the elastic fluid tested. Such behaviour could be explained by the following assumption: for moderates volumetric flow rate, elastic effects predominated and the vortices grew with the volumetric flow rate, eventually, for a certain volumetric flow rate the inertial forces became more significant than the elastic forces having as consequence that the vortex length decreased.

On the other hand, for the parabolic contraction the vortex enhancement was not found, this fact supported the idea that smooth contractions inhibits the genesis of secondary flows as it was observed by previous authors. Thus, the parabolic profile proposed by Naranjo (2010) fulfilled its primary objective of eliminating secondary flows resulting in better estimation of the extensional viscosity. In the case of Newtonian and Inelastic non-Newtonian fluids, flow separation was not observed even when the Binding's theory

suggested that it would happen at the beginning of the contraction for the Newtonian case (Eq. 29); for this reason Binding´s analysis can be consider a good approach.

For the elastic fluids, even when no secondary flow was observed, separation of the streamlines from the wall occurred in the presence of normal stresses. Therefore, to calculate the extensional viscosity according to Binding's analysis, the separation and non separation regions had to be considered when measuring the extensional viscosity to avoid high inaccuracies.

There were an almost free-vorticity and shear deformation nucleon at practically the entire length of the parabolic contraction soft at the thinnest part of the contraction where their magnitude became considerable; nevertheless, it could be no so important because the Binding's analysis considers the shear contributions to the measurements. Axial velocity and elongational rate exhibited first a fully developed behaviour and eventually it started growing in an exponential form at $z \approx$ 75 mm for all the volumetric flows for the elastic fluids. Dimensionless axial velocity showed a parabolic behaviour with respect to the dimensionless radius.

The experimental evidence suggested that parabolic contraction is useful for the measurements of the elongational viscosity of Newtonian, inelastic and elastic non-Newtonian fluids, however, for the third case the streamline separation has to be considered.

5.1. Future work and recommendations to the rheometer.

In order to be sure that the vortices don't appear at the parabolic contraction, a wider range of elastic fluids and Reynolds numbers have to be tested. A careful analysis of the flow separation conditions and experiments to observe the influence of the Deborah's number to the flow through the parabolic contraction have to be done. Besides, it would be useful to investigate at what point and under what conditions the inertial effects dominate the elastic effects as seen with the abrupt contraction.

Respect to the rheometer: From an experimental standpoint, the pressure drop could be measured between points along the parabola, so that the extensional viscosity would be estimated where the flow does not separate. In such case, the pressure transducer resolution should be as high as possible to ensure accurate results especially when working with low viscosity fluids. Another possibility could be changing the parabolic profile, specifically, the beginning where he parabola unites the wall by making it smoother obtaining with this that the angle of the contraction is lower than the natural angle of convergence of the flow. In that way, the separation of the streamlines could be avoided. Nevertheless, the manufacturing process would become more difficult because of the high length of the contraction. Using a semi-hyperbolic converging die, that has been proven to be useful in obtaining free-shear flow and constant elongational rates (Muñoz, 2011; Feigl *et al*, 2003), could be considered too. However, in those studies, fully-slip condition was considered and this could not be true physically unless the use of lubricants is considered which would bring more technical difficulties. In addition, experimental work should be done to validate then the semi-hyperbolic converging die.

REFERENCES

1. Afonso, A. and Pinho, F.T., "Numerical investigations of the velocity overshoots in the flow of viscoelastic fluids inside a smooth contraction "J. Non-Newtonian Fluid Mech, 139 (2006) 1-20.
2. Alves, M.A. and Poole, R.J., "Divergent flow in contractions" J. Non-Newtonian Fluid Mech, 144 (2007) 140-148.
3. Alves, M.A., Oliveira, P.J. and Pinho, F.T., "A convergent and universally bounded interpolation scheme for the treatment of advection" Int. J. Numer. Meth. Fluids, 41 (2003), 47-75.
4. Alves, M.A., Oliveira, P.J. and Pinho, F.T., "On the effect of contraction ratio in viscoelastic flow through abrupt contractions" J. Non-Newtonian Fluid Mech, 122 (2004), 117-130.
5. Alves, M.A., Pinho, F.T. and Oliveira, P.J., "Visualizations of Boger fluid flows in a 4:1 square-square contraction" AIChE Journal, 51 (2005), 2908-2922.
6. Ascanio, G., Carreau, P.J., Brito de la Fuente, E. and Tanguy, P.A. "Orifice flowmeter for measuring extensional rheological properties" Can. J. Chem. Eng., 80 (2002), 1189-1196.
7. Astarita, G. and Greco, G., "Excess pressure drop in laminar flow through sudden contraction. Newtonian liquids" Ind. Eng. Chem. Fundamentals, 7 (1968), 27-31.
8. Astarita, G., Greco, G. and Peluso L., "Excess pressure drop in laminar flow through sudden contraction. Non-Newtonian liquids" Ind. Eng. Chem. Fundamentals, 7 (1968), 595-598.
9. Baloch, A., Townsend, P. and Webster, M.F., "On vortex development in viscoelastic expansion and contraction flows", J. Non-Newtonian Fluid Mech, 65 (1996), 133-149.
10. Bariş, S., "Flow of an Oldroyd 8 constant fluid in a converging channel" Acta Mechanica, 148 (2001), 117-127.

11. Belbidia, F., Matallah, H. and Webster, M.F., ""Alternative subcell discretisations for viscoelastic flows: Velocity-gradient approximation" J. Non-Newtonian Fluid Mech, 151 (2008), 69-88.
12. Binding, D. M., “An approximate analysis for contraction and converging flows” J. Non-Newtonian Fluid Mech., 27 (1987), 173-189.
13. Clemeur, N., Rutgers, R.P.G. and Debbaut, B. "Numerical simulation of abrupt contraction flows using the Double Convected Pom-Pom model" J. Non-Newtonian Fluid Mech, 117 (2004), 193-209
14. Della Valle, D., Tanguy, P.A. and Carreau, P.J., "Characterization of the extensional properties of complex fluids using an orifice flowmeter" J. Non-Newtonian Fluid Mech, 94 (2000) 1-13.
15. Dorpinghaus, P.J. and Baird, D.G. "Pressure Profiles Along an Abrupt 4-1 Planar contraction" AIChE Journal, 49 (2003), 2487-2498.
16. Feigl, K., Tanner, F.X., Edwards, B.J. and Collier, J.R., "A numerical study of the measurement of elongational viscosity of polymeric fluids in a semihyperbolically converging die" J. Non-Newtonian Fluid Mech, 115 (2003) 191-215
17. Hertel, D., Valette, R. and Münstedt, H., "Three-dimensional entrance flow of a low-density polyethylene (LDPE) and a linear low-density polyethylene (LLDPE) into a slit die" J. Non-Newtonian Fluid Mech, 153 (2008) 82-94.
18. Liang, Ji-Zhao, "Estimation of entry natural converging angles during capillary extrusion flow of carbon black filled NR/SBR compound" Polymer Testing, 24 (2005), 435-438.
19. Lubansky, A.S., Boger, D.V, Servais, C., Burbidge A.S. and Cooper-White, J.J., "An approximate solution to flow through a contraction for high Trouton ratio fluids" J. Non-Newtonian Fluid Mech, 144 (2007) 87-97.
20. Martyn, M.T., Nakason, C. and Coates, P.D., "Flow visualization of polymer melts in abrupt contraction extrusion dies: quantification of melt recirculation and flow patterns" J. Non-Newtonian Fluid Mech, 91 (2000) 109-122.

21. Mitsoulis, E. and Hatzikiriakos, S.G., "Bagley correction: the effect of contraction angle and its prediction" Rheol. Acta, 42 (2009), 309-320.
22. Mitsoulis, E., Schwetz, M. and Münstedt, "Entry flow of LDPE melts in a planar contraction" J. Non-Newtonian Fluid Mech, 111 (2003) 41-61.
23. Mongruel, A. and Cloitre, M., "Axisymmetric orifice flow for measuring the elongational viscosity of semi-rigid polymer solutions" J. Non-Newtonian Fluid Mech, 110 (2003) 27-43.
24. Muñoz, Enrique “” PhD Thesis, (2011).
25. Naranjo, J., "Desarrollo y construcción de un reómetro de orificio para determinar propiedades extensionales" PhD. Thesis, (2010).
26. Nigen, S. and Walters, K., "Viscoelastic contraction flows: comparison of axisymmetric and planar configurations" J. Non-Newtonian Fluid Mech, 102 (2002) 343-359.
27. Nigen, S., Kissi, N. El, Piau, J.-M. and Sadun, S., "Velocity field for polymer melts extrusion using particle image velocimetry. Stable and unstable regime" J. Non-Newtonian Fluid Mech, 177 (2003) 177-202.
28. Oliveira, M.S., Alves, M.A., Pinho, F.T. and McKinley, G.H., "Viscous flow through microfabricated hyperbolic contractions" Exp. Fluids, 43 (2007), 437-451.
29. Olson, D.J. and Fuller, G.G., "Contraction and expansion flows of a Langmuir monolayers" J. Non-Newtonian Fluid Mech, 89 (2000) 187-207.
30. Poole, R.J., Escudier, M.P. and Oliveira, P.J., "Laminar flow of a viscoelastic shear-thinning liquid through a plane sudden expansion precede by a gradual contraction" Proc. R. Soc. A, 461 (2005), 3827-3845.
31. Poole, R.J., Escudier, M.P., Afonso, A. and Pinho, F.T., "Laminar flow of a viscoelastic shear-thinning liquid over a backward-facing step preceded by a gradual contraction" Physics of Fluids, 19 (2007), 093101.

32. Rodd, L.E., Cooper-White, J.J., Boger, D.V. and McKinley, G.H., "Role of the elasticity number in the entry flow of dilute polymer solutions in micro-fabricated contraction geometries" J. Non-Newtonian Fluid Mech, 143 (2007), 170-191.
33. Rothstein, J.P. and McKinley G.H., "Extensional flow of a polystyrene Boger fluid through a 4:1:4 axisymmetric contraction/expansion" J. Non-Newtonian Fluid Mech, 86 (1999) 61-88.
34. Rothstein, J.P. and McKinley, G.H., "The axisymmetric contraction–expansion: The role of extensional rheology on vortex growth dynamics and the enhanced pressure drop" J. Non-Newtonian Fluid Mech, 98 (2001), 33-63.
35. Sadri, R.M.and Floryan J.M., "Entry flow in channel" Computers and Fluids, 31 (2002), 133-157.
36. Shirakashi, M., Ito, H. and James, D.F., "LVD measurement of the flow field in a constant-extensional-rate channel" J. Non-Newtonian Fluid Mech, 74 (1998), 247-262.
37. Tremblay, B., "Estimation of the elongational viscosity of polyethylene blends at high deformation rates" J. Non-Newtonian Fluid Mech, 33 (1989), 137-164.